Verification of the Current Coupling Collision Probability Method with Orthogonal Flux Expansion for the Assembly Calculations

Dzianis Litskevich[a)1], Seddon Atkinson[a)], Sebastian Davies[a)]

[a)] *School of Engineering, University of Liverpool, Brownlow Hill, Liverpool, L69 3GH, UK*

Abstract

The operation of nuclear reactors requires detailed knowledge of important safety parameters, such as the spatial power distribution, control rod worth, margin to departure from nucleate boiling (DNB), fuel pin burnup etc. To obtain a detailed analysis of all of the safety parameters requires a full core pin-by-pin coupled neutronics and thermal-hydraulics simulations which are too computationally expensive even for modern high-performance computer clusters. Therefore, the industrial standard approach in design and safety calculations are coupled neutronics and thermal-hydraulics codes for the steady state and transient simulations. In these codes, the neutronics calculations are typically performed at a nodal level using the diffusion approximation and assembly-homogenised sets of cross-sections while the thermal hydraulics relies on a channel model with fuel assembly sized channels. However, for determining safety limits, which are based on local pin-based parameters, the knowledge of the power and temperature distribution on a nodal level is not sufficient. Therefore, novel new approaches are required to resolve this multiscale and multiphysics problem to resolve the power distribution within the zones of interest. Pin-wise calculations, in this case, are performed by applying a transport solver using the heterogeneous fuel assembly geometry on an unstructured mesh with boundary conditions extracted from the 3D full core nodal diffusion solution. This combined nodal-transport approach will provide the detailed power distribution on the pin-level and perform coupled multiphysics simulations within reasonable simulation time limits, which is important for industry.

To follow this strategy, a transport solver is required which can be used for the flux reconstruction on the pin level. Current coupling collision probability (CCCP) method seems to be a good choice for the development of such a solver.

In this study, the developed transport solver utilising CCCP method with orthogonal flux expansion is tested and verified on the set of the benchmark problems. The results of simulations are compared with the results of Monte Carlo and deterministic code. The expansion of the flux by orthogonal polynomials allows us to avoid discretisation of the calculation regions while keeping the accuracy of the calculations to an acceptable level. The results of the calculations demonstrate good agreement with the results of Monte Carlo calculations. The comparison of the new method with the flat flux (today's industry standard approach) approximation demonstrates either an improved quality of the result for identical cell discretisation or reduced computational time to achieve the identical solution.

Keywords: *Neutron Transport, Current Coupling Collision Probabilities, Orthogonal Polynomials*

[1] Corresponding author. E-mail: d.litskevich@liverpool.ac.uk

Nomenclature

The acronyms in the overall text have an associated meaning given in the following table.

Acronym	Full Description
DYN3D	Dynamical 3 Dimensional
CASL	Consortium for Advanced Simulation of Light water Reactors
DRD	Digital Reactor Design
NURESAFE	Nuclear Reactor Safety Simulation Platform
CCCP	Current Coupling Collision Probability
CCCPO	Current Coupling Collision Probability with Orthogonal Flux Expansion
PWR	Pressurised Water Reactor
MOX	Mixed Oxide
KAIST	Korea Advanced institute of Science and Technology
MIT	Massachusetts Institute of Technology
EPSRC	Engineering and Physical Sciences Research Council
LWR	Light Water Reactor

The symbols in the overall text have an associated meaning given in the following table.

Symbol	Description
g	Index of the energy group
i, i'	Indices of the spatial regions
k, k'	Indices of the spatial modes
s	Index of the cell's side
n	Index of the segment
m	Index of the azimuthal sector
l	Index of the polar sector
N_i	Total number of the regions in the cell
N_k	Total number of the spatial modes
N_s	Total number of the cell's sides
N_n	Total number of the cell's segments
N_m	Total number of the azimuthal sectors
N_l	Total number of the polar sectors
N_g	Total number of energy groups
Σ_i	Total cross section in the region i
$\Sigma_{s,i,g'\to g}$	Scattering cross section from group g' to group g in the region i
$\nu\Sigma_{f,i,g}$	Production cross section in the group g, region i
χ_g	Value of the fission spectrum for the group g
k_{eff}	Effective multiplication factor
A_i	Volume of the i-th region
$\Phi_{i,k}$	Neutron flux in region i, spatial mode k
$\Phi_{g,i,k}$	Neutron flux in group g, region i, spatial mode k
$Q_{i,k}$	Neutron source in the region i, spatial mode k
$Q_{g,i,k}$	Neutron source in the region i, spatial mode k, group g

$Q_{g,i,k}^{ext}$	External source in the region i, group g, spatial mode k
$U_{i',k'\to i,k}$	Probability for the neutron born within region i', spatial mode k' to have its first collision in the region i, spatial mode k
$\gamma_{s,n,m,l\to i,k}$	Probability for neutron entering the cell via side s, segment n, azimuthal sector m and polar sector l to have its first collision within region i, spatial mode k
$\upsilon_{i,k\to s,n,m,l}$	Probability for neutron born in the region i, spatial mode k to leave cell without collision via side s, segment n, azimuthal sector m and polar sector l
$\beta_{s',n',m',l\to s,n,m,l}$	Probability for the neutron entering cell via side s', segment n', azimuthal sector m' and polar sector l to leave the cell via side s, segment n, azimuthal sector m and polar sector l
$J_{s,n,m,l}^{in}$	Input neutron current on the cell's side s, segment n, azimuthal sector m and polar sector l
$J_{s,n,m,l}^{out}$	Output neutron current on the cell's side s, segment n, azimuthal sector m and polar sector l
$\boldsymbol{\Phi}$	Flux column-vector
$\boldsymbol{Q}$	Source column-vector
$\boldsymbol{J^{in}}$	Input current column-vector
$\boldsymbol{J^{out}}$	Output current column-vector
$\boldsymbol{U}$	Region-to-region collision probability matrix
$\boldsymbol{\Gamma}$	Surface-to-region collision probability matrix
$\boldsymbol{V}$	Region-to-surface escape probability matrix
$\boldsymbol{B}$	Surface-to-surface transmission probability matrix
$\boldsymbol{H}$	Connectivity matrix
ε	Convergence criteria for the currents
ε_e	Convergence criteria for the eigenvalues

1. Introduction

Safe and reliable operation of the nuclear power plants requires detailed knowledge of the important safety related parameters such as spatial distribution of the temperatures, water densities and neutron fluxes within the reactor core. 3D nodal diffusion codes (such as PANTHER [1], DYN3D [2]) are the main tool for the safety evaluation of the nuclear power plants. Due to their efficiency and comparable good accuracy, these codes are widely used both in academia and industry. Modern nodal codes can solve 3D coupled thermal hydraulic and neutronics tasks quickly and efficiently. In order to achieve this, the reactor core is discretised into the set of the nodes usually square or hexagonal prisms. Within each node neutronics cross sections are supposed to be uniform and neutron fluxes can be represented using analytical or polynomial function expansions preserving transverse leakages. The thermal hydraulics relies on a channel model with the fuel assembly sized channels. The outcome of the nodal codes is node averaged physical parameters such as temperatures of fuel, cladding, moderator, water density, neutron fluxes, etc. However, for determining safety limits, which are based on local pin-based parameters, the knowledge of the power and temperature distribution on a nodal level is not sufficient. Therefore, in practice, additional conservative coefficients are applied to ensure that the safety related parameters are kept within safety limits. The conservative approach leads to reduced operational productivity of the nuclear power plant which can cause significant loss of revenue and therefore an increase in energy prices. Therefore, it is of high interest to evaluate safety related parameters avoiding excessive conservatism. In order to reduce these safety margins and provide a higher understanding of the underlying physics inside the reactor several projects, such as CASL [3], DRD [4], NURESAFE [5] were commissioned in different countries through over the world in the recent years.

The ideal scenario would be 3D full core pin-by-pin coupled multiphysics simulation of the nuclear power plant. Unfortunately, the computational demands for such a task is very high. Even modern supercomputers require thousands of the core-hours to simulate a few seconds of transient behaviour [6]. Therefore, at the current stage such high fidelity tools are very promising and scientifically highly interesting cannot be applied to routine day-to-day industrial application.

In order to bring high fidelity simulation tools into industrial applications, another approach is proposed. This approach implies that the multiscale and multiphysics approach can be used selectively to resolve the power distribution within the zones of interests (for example, hottest assembly). Pin-wise calculations, in this case, are performed by applying a transport solver using the heterogeneous fuel assembly geometry on an unstructured mesh with boundary conditions extracted from the 3D full core nodal diffusion solution [7]–[9]. This combined nodal-transport

approach potentially allows for the detailed power distribution on the pin-level to be obtained and performs coupled multiphysics simulations within reasonable simulation time while avoiding the use of the supercomputers which is important for industrial use.

An important part of such a multi-physical tool will be neutron transport solver capable of solving the multigroup transport equation fast and accurately on the assembly level. It is obvious that the accuracy of the flux reconstruction within assembly will be strongly dependent on the boundary conditions used for such reconstruction. Therefore, additional requirements to such a solver would be possibility for flexible treatment of the boundary conditions (for example, cell dependent albedos). The Current Coupling Collision Probability (CCCP) method [10]–[12] fulfils both mentioned requirements. In this method, the computational domain is subdivided on a set of heterogeneous regions. The heterogeneous space regions are coupled into the full system by interface currents with a discretised angular dependence. Within heterogeneous regions the neutron transport equation is solved by collision probabilities method. CCCP allows for the resolution of the neutron transport problem on the unstructured mesh fast and efficiently (CCCP-based code HELIOS [13] is used for the cross sections generations) and due to the nature of the methodology, boundary conditions treatment can be very flexible.

Previously, CCCP solver with orthogonal expansion of flux was developed and tested for the single cell one group fixed source problems [14]. In the current study, the solver was extended for the case of the unstructured 2D assemblies, multiple groups and eigenvalue problems.

This paper is organised as follows. Section 2 describes the methodology used in the multigroup transport solver. Section 3 introduces the description of the benchmark problems used for verification of the developed solver. Section 4 presents results of the developed solver calculations and comparison with the reference Monte Carlo solutions. Finally, Section 5 presents our conclusions.

2. Methodology

In the previous studies [11], [15], the modification of the CCCP method was proposed for regular hexagonal geometry. In contrast to the conventional CCCP method where flat flux approximation is used to represent the neutron flux and sources within computational regions, the proposed modification takes into account spatial dependency of the fluxes (sources) by utilising Current Coupling Collision Probability with Orthogonal flux expansion (CCCPO). This approach allows for fewer computational regions while maintaining the accuracy to a high level and removes the requirement for users to manually subdivide the regions into subzones [16]. The methodology

was extended for the case of the irregular meshes and tested for the case of the single cells [14]. In the current study, the neutron transport solver was extended for the case of the 2D unstructured meshes, fixed source and eigenvalue problems.

2.1. Formulation of the CCCPO method for the set of the cells

Before proceeding to the presentation of the methodology, we would like to clarify the meaning of some terms that will be used further in this study. We assume, that the computational domain can be subdivided on the set of the "cells". Under the term "cell" we mean the region surrounded by N-sided polygon with (or without) inscribed concentric circles as it is shown in Figure 1.

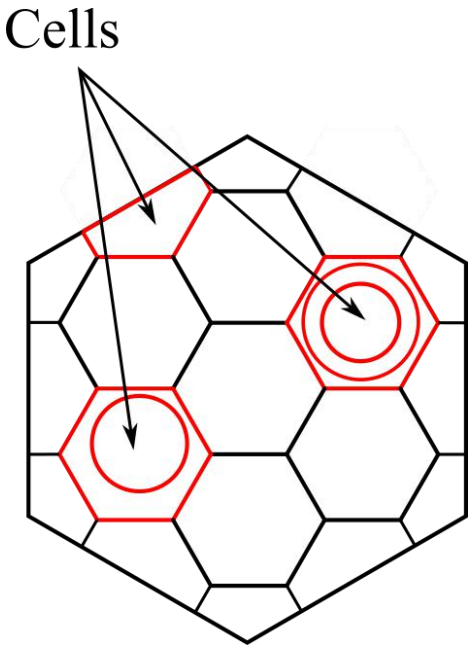

Figure 1. Different types of the cells in the assembly

The main idea utilising by CCCP (and CCCPO) methodology is discretisation of the computational domain on a set of heterogeneous regions. The heterogeneous space regions are coupled into the full system by interface currents with a discretised angular dependence. The neutron transport equation is solved by collision probabilities method within heterogeneous regions. The solution of the neutron transport equation starts from the evaluation of the first flight collision probabilities: surface-to-surface transmission probability, region-to-surface and surface-to-region collision probabilities, region-to-region collision probability. In order to take into account nonuniformity of the angle distribution of the neutron current, the directional semi sphere is subdivided on the polar and azimuthal sub angles (sectors) in the same way as it has been done in HELIOS code [10]. The spatial nonuniformity of the neutron currents on the sides of the cell are considered by subdivision of the sides on the segments. Therefore, region-to-surface, surface-to-

region and surface-to-surface probabilities are defined for the cell side, side's segment, polar sector and azimuthal sector. In contrast to the CCCP method, in the CCCPO method, region-to-surface, surface-to-region and region-to-region collision probabilities depend, in addition, on the spatial modes of the flux. Collision probabilities are integrated using ray-tracing method for each type of the cell within assembly. The methodology of integration is described in details in the literature [9], [10], [17].

After evaluation of the collision probabilities, the fluxes within calculation regions are evaluated using the neutron balance equations which can be written in the following way (the energy group index g is omitted):

$$\Sigma_i A_i \Phi_{i,k} = \sum_{i'=1}^{N_i} \sum_{k'=1}^{N_k} U_{i',k' \to i,k} Q_{i',k'} A_{i'} + \sum_{s=1}^{N_s} \sum_{n=1}^{N_n} \sum_{m=1}^{N_m} \sum_{l=1}^{N_l} \gamma_{s,n,m,l \to i,k} J^{in}_{s,n,m,l} \quad (1)$$

Where A_i is the volume of the i-th region; Σ is the total cross-section; $\Phi_{i,k}$ is the neutron flux in region i, spatial mode k; $U_{i',k' \to i,k}$ is the probability for the neutron born within region i', spatial mode k' to have its first collision in the region i, spatial mode k; $Q_{i,k}$ is the neutron source in the region i, spatial mode k; $\gamma_{s,n,m,l \to i,k}$ is the probability for neutron entering the cell via side s, segment n, azimuthal sector m and polar sector l to have its first collision within region i, spatial mode k; $J^{in}_{s,n,m,l}$ is the input neutron current on the cell's side s, segment n, azimuthal sector m and polar sector l.

The response output current is defined by the neutron sources within the regions of the cell and input neutron current on the cell's borders.

$$J^{out}_{s,n,m,l} = \sum_{i=1}^{N_i} \sum_{k=1}^{N_k} \nu_{i,k \to s,n,m,l} Q_{i,k} A_i + \sum_{s'=1}^{N_s} \sum_{n'=1}^{N_n} \sum_{m'=1}^{N_m} \sum_{l=1}^{N_l} \beta_{s',n',m',l \to s,n,m,l} J^{in}_{s',n',m',l} \quad (2)$$

Where $J^{out}_{s,n,m,l}$ is the output neutron current on the cell's side s, segment n, azimuthal sector m and polar sector l; $\nu_{i,k \to s,n,m,l}$ is the probability for neutron born in the region i, spatial mode k to leave cell without collision via side s, segment n, azimuthal sector m and polar sector l; $\beta_{s',n',m',l \to s,n,m,l}$ is the probability for the neutron entering cell via side s', segment n', azimuthal sector m' and polar sector l to leave the cell via side s, segment n, azimuthal sector m and polar sector l.

Finally, assuming specular boundary conditions on the sides of the cell, the relation between input and output currents can be written:

$$J^{in}_{s,n,m,l} = J^{out}_{s,n,m,l} \tag{3}$$

In the current study, two types of the problems are considered – fixed source problem and eigenvalue problem. Depending on the type of the problem (fixed source or eigenvalue) the sources in the equations (1) and (2) are calculated in a slightly different way. In the case of the eigenvalue problem, the source for the energy group g, region i and spatial mode k is evaluated according to the following expression:

$$Q_{g,i,k} = \chi_g \frac{1}{k_{eff}} \sum_{g'=1}^{N_g} \nu\Sigma_{f,g,i}\Phi_{g',i,k} + \sum_{g'=1}^{N_g} \Sigma_{s,i,g'\to g}\Phi_{g',i,k} \tag{4}$$

Where χ_g is the value of the fission spectrum for the group g; k_{eff} is the effective multiplication factor; N_g is the total number of the energy groups; $\nu\Sigma_{f,i,g}$ is the production cross section in the group g, region i; $\Sigma_{s,i,g'\to g}$ is the scattering cross section from group g' to group g in the region i. In the case of the non-multiplying medium fixed source problem, the neutron source within computational regions is evaluated according to the following equation:

$$Q_{g,i,k} = \sum_{g'=1}^{N_g} \Sigma_{s,i,g'\to g}\Phi_{g',i,k} + Q^{ext}_{g,i,k} \tag{5}$$

Where $Q^{ext}_{g,i,k}$ is the external source in the region i, group g, spatial mode k.

The equations (1) and (2) presented above can be written in the matrix form (for a single cell and energy group g):

$$\begin{pmatrix} \varphi_1 \\ \vdots \\ \varphi_{N_{ik}} \end{pmatrix} = \begin{pmatrix} u_{1,1} & \cdots & u_{1,N_{ik}} \\ \vdots & \ddots & \vdots \\ u_{N_{ik},1} & \cdots & u_{N_{ik},N_{ik}} \end{pmatrix} \begin{pmatrix} q_1 \\ \vdots \\ q_{N_{ik}} \end{pmatrix} + \begin{pmatrix} \gamma_{1,1} & \cdots & \gamma_{1,N_{snml}} \\ \vdots & \ddots & \vdots \\ \gamma_{N_{ik},1} & \cdots & \gamma_{N_{ik},N_{snml}} \end{pmatrix} \begin{pmatrix} j^{in}_1 \\ \vdots \\ j^{in}_{N_{snml}} \end{pmatrix} \tag{6}$$

$$\begin{pmatrix} j^{in}_1 \\ \vdots \\ j^{in}_{N_{snml}} \end{pmatrix} = \begin{pmatrix} \nu_{1,1} & \cdots & \nu_{1,N_{ik}} \\ \vdots & \ddots & \vdots \\ \nu_{N_{snml},1} & \cdots & \nu_{N_{snml},N_{ik}} \end{pmatrix} \begin{pmatrix} q_1 \\ \vdots \\ q_{N_{ik}} \end{pmatrix} + \begin{pmatrix} \beta_{1,1} & \cdots & \beta_{1,N_{snml}} \\ \vdots & \ddots & \vdots \\ \beta_{N_{snml},1} & \cdots & \beta_{N_{snml},N_{snml}} \end{pmatrix} \begin{pmatrix} j^{in}_1 \\ \vdots \\ j^{in}_{N_{snml}} \end{pmatrix} \tag{7}$$

The length N_{ik} of the column-vectors $\vec{\phi}$ and $\vec{q}$ is defined by the number of the computational regions and number of spatial modes within the regions. For example, in the case of 3 computational regions and 1 spatial mode (flat flux approximation) N_{ik} will be equal to 3 (3x1); in the case of the 3 spatial modes within each computational region, N_{ik} will be equal to 9 (3x3)

and so on. The length N_{snml} of the column-vectors $\vec{j}^{in}$ and $\vec{j}^{out}$ are defined by the number of sides, segments and angular sectors. For example, in the case of the uniform subdivision of the sides of the regular polygon, $N_{snml} = N_n N_s N_m N_l$, where N_n is the number of the segments, N_s is the number of sides, N_m is the number of the azimuthal angles and N_l is the number of the polar angles.

The equations (6) and (7) can be written in a shorter notation:

$$\boldsymbol{\Phi} = \boldsymbol{U}\boldsymbol{Q} + \boldsymbol{\Gamma}\boldsymbol{J}^{\boldsymbol{in}} \tag{8}$$

$$\boldsymbol{J}^{\boldsymbol{out}} = \boldsymbol{V}\boldsymbol{Q} + \boldsymbol{B}\boldsymbol{J}^{\boldsymbol{in}} \tag{9}$$

$$\boldsymbol{J}^{\boldsymbol{in}} = \boldsymbol{J}^{\boldsymbol{out}} \tag{10}$$

The equations (8) – (11) are written for the single cell with the reflective boundary condition. In order to complete the formulation, we note that the currents leaving one cell enter another. Therefore, for the set of the cells coupled by the currents, the following relation can be written for the input and output currents:

$$\widetilde{\boldsymbol{J}}^{\boldsymbol{out}} = \boldsymbol{H}\widetilde{\boldsymbol{J}}^{\boldsymbol{in}} \tag{11}$$

Where $\widetilde{\boldsymbol{J}}^{\boldsymbol{in}}$ and $\widetilde{\boldsymbol{J}}^{\boldsymbol{out}}$ are "global" input and output neutron current vectors defined for all the cells in the system; $\boldsymbol{H}$ is the connectivity matrix. This matrix reflects the connectivity between input and output currents of the cells in the system and includes boundary conditions on the outer surface.

2.2. Within group iterations

The system of the linear algebraic equations defined by the equations (8) - (11) is solved using conventional inner-outer iteration scheme. The iteration scheme used in the current study is very similar to the iteration scheme used in the HELIOS code [13]. The inner iterations are performed to evaluate the currents within a given group using equations (9) and (11). It is assumed that the neutron source and input currents are known. They are passed into the inner iteration subroutine either as initial guess (for the very first iteration) or as sources and input currents calculated on the previous iteration. All the cells in the system are numbered and connectivity matrix is created as preliminary step. The iteration process starts from the first cell and goes until the last cell. The updated output currents are evaluated using equation (9). The updated output currents overwrite existing values as soon as they have been obtained. This approach is typical for Gauss-Seidel scheme of iterations [18]. In the current version of the solver there is no relaxation techniques applied (i.e. relaxation parameter ω is equal to 1). However, in the future versions of the

program they can be implemented to speed up the convergence of the currents. The iterations continue until the convergence criteria given by equation (12) is met or the maximal number of inner iterations (set in the input file) is reached.

$$|j^n - j^{n-1}| < \varepsilon \tag{12}$$

Where j^n and j^{n-1} are the currents of the n-th and $(n-1)$-th iterations respectively; ε is the convergence criteria which is set in the input file. When the inner iterations are performed for each energy group, fluxes within the computational regions are evaluated using (9). It should be noted that the matrices $\boldsymbol{B}, \boldsymbol{V}$, $\boldsymbol{\Gamma}$ and $\boldsymbol{U}$ grows and become sparse as number of the segments, polar and azimuthal sectors increase. Therefore, to reduce the memory requirements these matrices are stored as sparse matrices (i.e. only non-zero elements and arrays with the appropriate indices are stored in memory). The same technique is applied for the connectivity matrix $\boldsymbol{H}$.

2.3. Eigenvalue iterations

The flowchart of the eigenvalue calculation is shown in Figure 2.

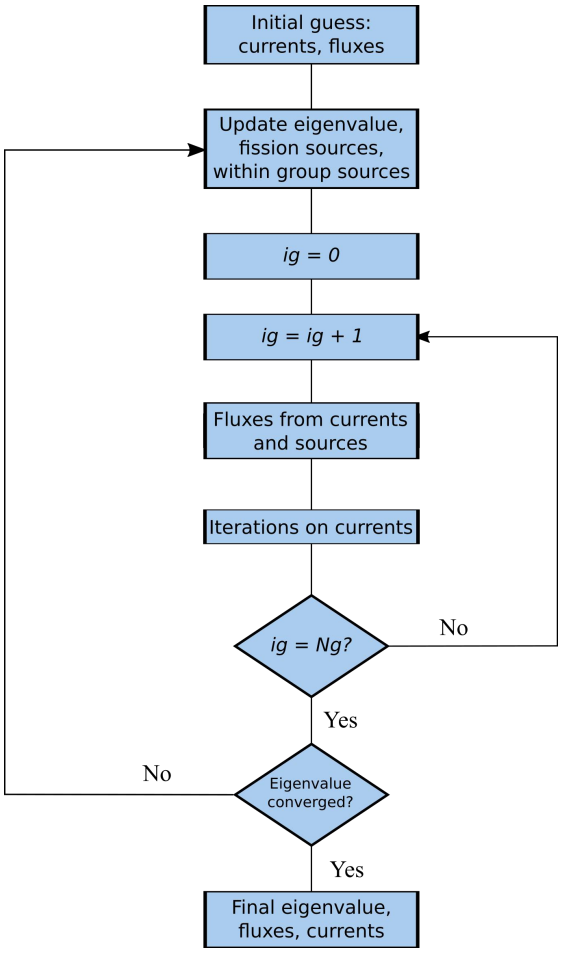

Figure 2. Flowchart of the eigenvalue iterations

The very first eigenvalue iteration starts from the initial guess of the current, sources and effective multiplication factor. The within groups sources are calculated using equation (4) for each calculation region. The iterations of currents are performed for each energy group. When they are finished, the convergence criteria for the eigenvalue is checked. In the current version of the transport solver, the effective multiplication factor is calculated for each region containing fissile material as:

$$k_{eff,i}^{n} = \frac{Q_{f,i}^{(n)}}{Q_{f,i}^{(n-1)}} \tag{13}$$

Where $k_{eff.i}^{n}$ is the multiplication factor for the region i of n-th iteration; $Q_{f,i}^{(n-1)}$ is the fission source for the region i of (n-1)-th iteration and $Q_{f,i}^{(n)}$ is the fission source for the region i of n-th iteration. As can be observed from the equation (13), the effective multiplication factor is defined for each region containing fissile material. Therefore, the eigenvalue of the system is defined as:

$$k_{eff} = \frac{1}{2}(k_{eff,max} + k_{eff,min}) \tag{14}$$

Where $k_{eff,max}$ and $k_{eff,min}$ are maximal and minimal values of the multiplication factors in the system. As iteration process converges, the difference between maximal and minimal multiplication factors tends to zero. The convergence criteria for the eigenvalue iterations is defined by the following relations:

$$|\, k_{eff,max} - k_{eff,min}| < \varepsilon_e \text{ and } |k_{eff}^{(p)} - k_{eff}^{(p-1)}| < \varepsilon_e \tag{15}$$

Where $k_{eff}^{(p)}$ is the effective multiplication factor of the system of p-th iteration; $k_{eff}^{(p-1)}$ is the effective multiplication factor of $(p-1)$-th iteration; ε_e is the eigenvalue convergence criteria which is by default set to $0.5 \cdot 10^{-6}$ but can be changed in input file. This scheme allows for the avoidance of situations when the difference between previous and current iteration is smaller than ε_e but convergence has not been yet achieved.

3. Description of the Benchmark Problems

The developed transport solver was tested on the number of benchmark problems. The input data for some of them were taken from the well-known benchmarks and some of the problems were specially designed for the verification of the neutron transport solver. In the current chapter the description of the benchmark problems used in this study is presented.

3.1. One group fixed source mini assemblies

This benchmark was proposed by authors. This is one group fixed source benchmark which is used for the evaluation of possibility of the developed neutron transport solver accurately calculate spatial distribution of the neutron flux within the fuel assembly. Two types of hypothetical mini assemblies were considered in the current study: regular square assembly with absorber and regular hexagonal assembly with the gap (with absorber cell). The material maps for both assemblies are presented in Figure 3 and Figure 4.

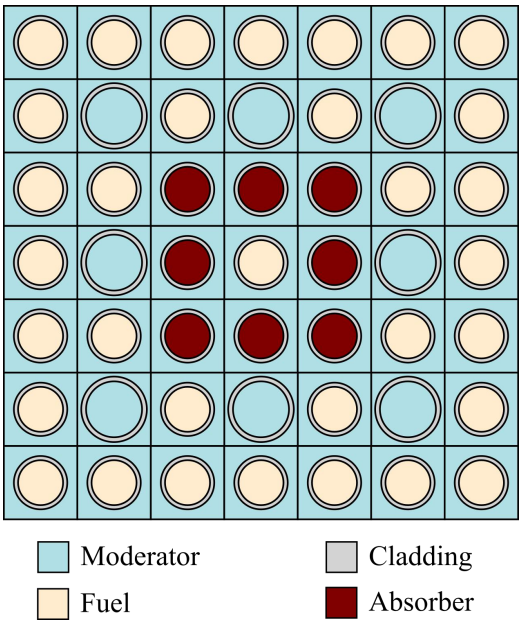

Figure 3. Material map for the fixed source square assembly problem

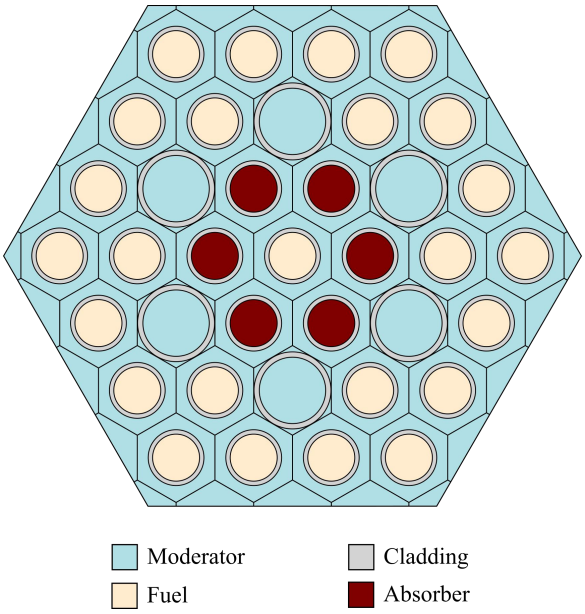

Figure 4. Material map for the fixed source hexagonal assembly problem

The arrangement of the materials within assemblies is quite artificial and does not completely reflect arrangement of the materials in the real fuel assemblies. However, for the test purposes, this arrangement, in our view, is a good choice since it represents:

1. Highly heterogeneous system
2. Different geometries of the cells
3. Unstructured mesh (see gap cells in the hexagonal assembly)
4. It is expected that the high gradient of the neutron flux will take place in the central fuel cell surrounded by the absorber cells. It can be challenging to reproduce the shape of the flux correctly.

Different type of the cells in the hexagonal and square assemblies are shown in Figure 5.

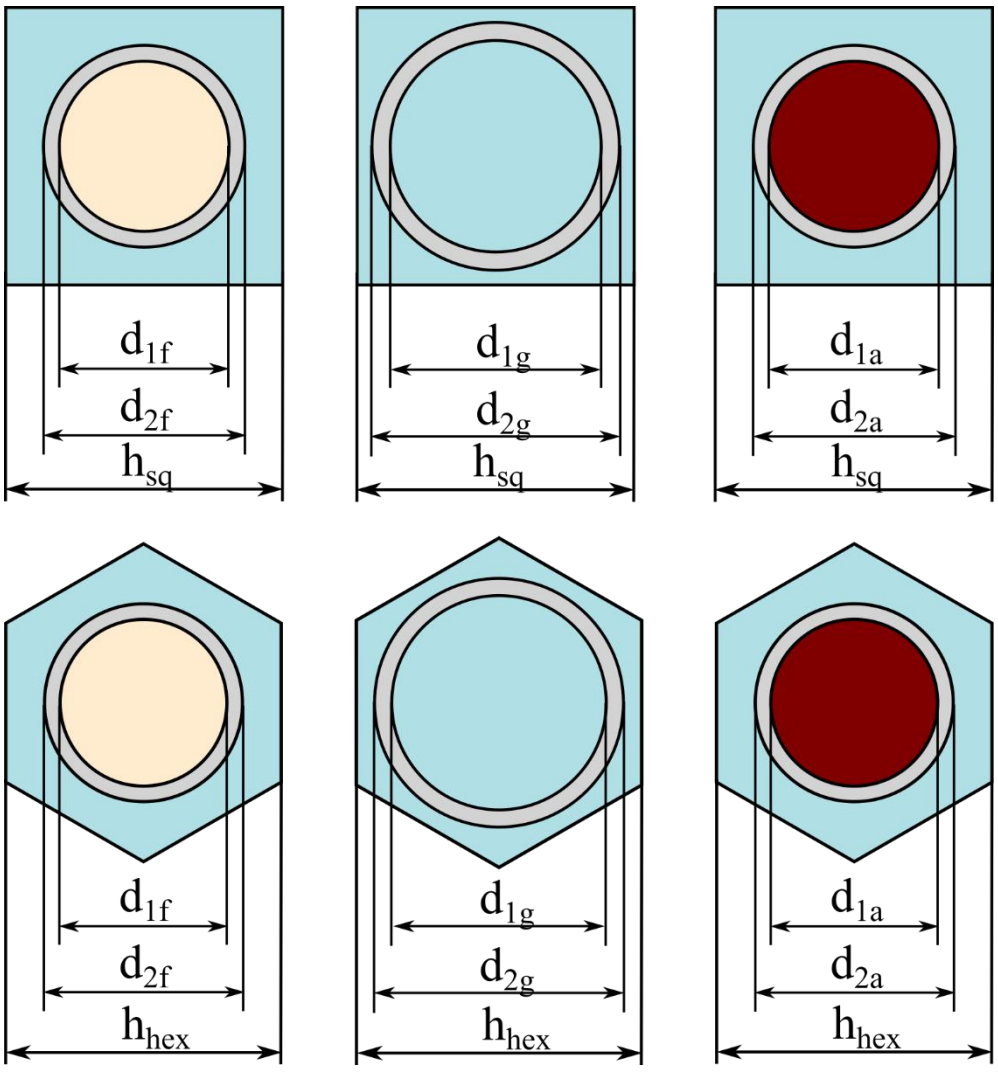

Figure 5. Geometries of the square (top) and hexagonal (bottom) cells

Spatial dimensions of the square and hexagonal cells are presented in Table 1.

Table 1. Spatial sizes of the cells

Radii/pitch	Square cell	Hexagonal cell
R_{1f}, cm	0.3860	0.3860
R_{2f}, cm	0.4582	0.4582
R_{1g}, cm	0.4800	0.5450
R_{2g}, cm	0.5626	0.6323
R_{1a}, cm	0.3860	0.3860
R_{2a}, cm	0.4582	0.4582
h_{sq}, cm	1.260	
h_{hex}, cm	1.275	

The pitch of the hexagonal assembly is equal to 8.22 cm while assembly pitch of the square assembly is 8.82 cm. Both square and hexagonal fixed source problems are one group problems and none of the materials had fission cross sections. The cross sections used for the simulations are summarised in Table 2.

Table 2. Cross sections of the materials

XS type	Fuel	Cladding	Absorber	Moderator
Σ_t, cm^{-1}	0.63	0.276	10.0	1.5
Σ_s, cm^{-1}	0.33	0.272	0.3	1.425

The neutron source with the density 1.0 cm^{-1} is distributed uniformly within the moderator material.

3.2. C5G7 hexagonal MOX assembly

The hexagonal extension of the 2D C5G7 benchmark [19] was chosen to test the capability of the solver to simulate eigenvalue multigroup problems for the realistic geometries and material compositions. In the current study single MOX assembly was chosen for test purposes. The geometrical configuration and material map of the assembly are presented in Figure 6.

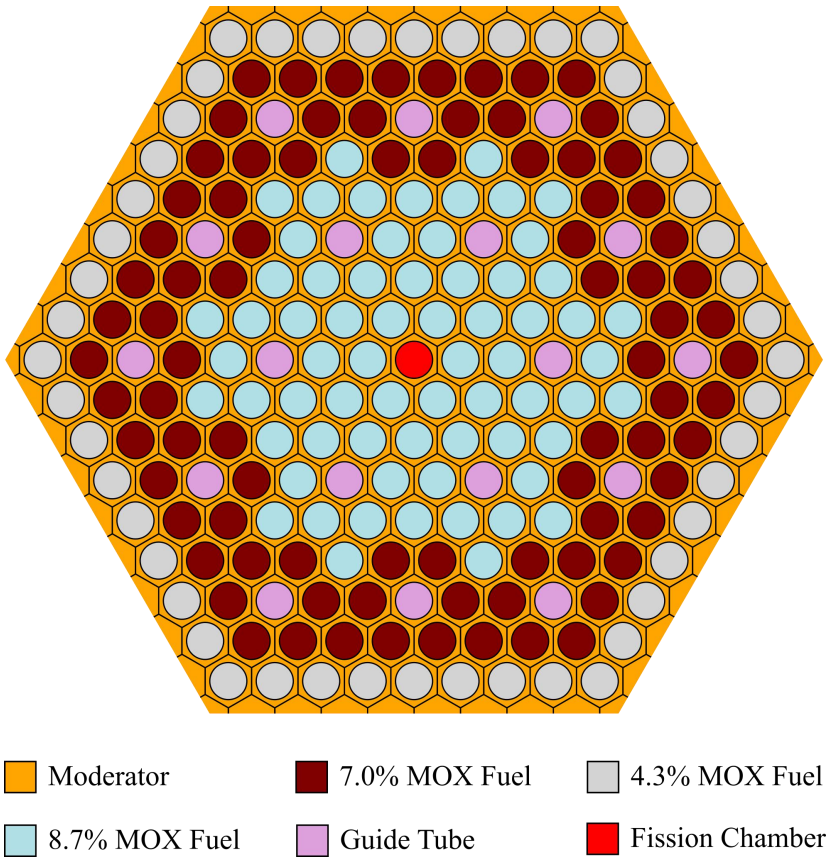

Figure 6. Material map of the hexagonal C5G7 MOX assembly

The assembly consists of 9 rows filled with the same materials as for the conventional C5G7 MOX assembly. The side of the cell in the lattice is equal to 0.78 cm and assembly pitch ~20.61 cm. Further details of the benchmark (such as neutron cross sections, radii of the pins, etc.) can be found in the literature [19]. The system was simulated with reflective boundary conditions.

3.3. KAIST 1A MOX Assembly

The developed neutron transport solver is intended to be used for the simulation of the real reactor assemblies. The multigroup cross sections for the neutron transport solver can be prepared using lattice codes (such as HELIOS, SCALE or continuous energy Monte Carlo codes). KAIST 1A benchmark [20] was chosen to test the possibility of the developed neutron transport solver to model such a problem.

The KAIST 1A benchmark is a small MOX-loaded core, basically a simplified small core PWR problem. The reactor core consists of 52 assemblies with the thermal power 900 MWth. The core consists of the both uranium oxide and MOX fuel assemblies. In the current study, MOX assembly without burnable absorbers and control rods was chosen for analysis. The material map of the MOX fuel assembly is presented in Figure 7.

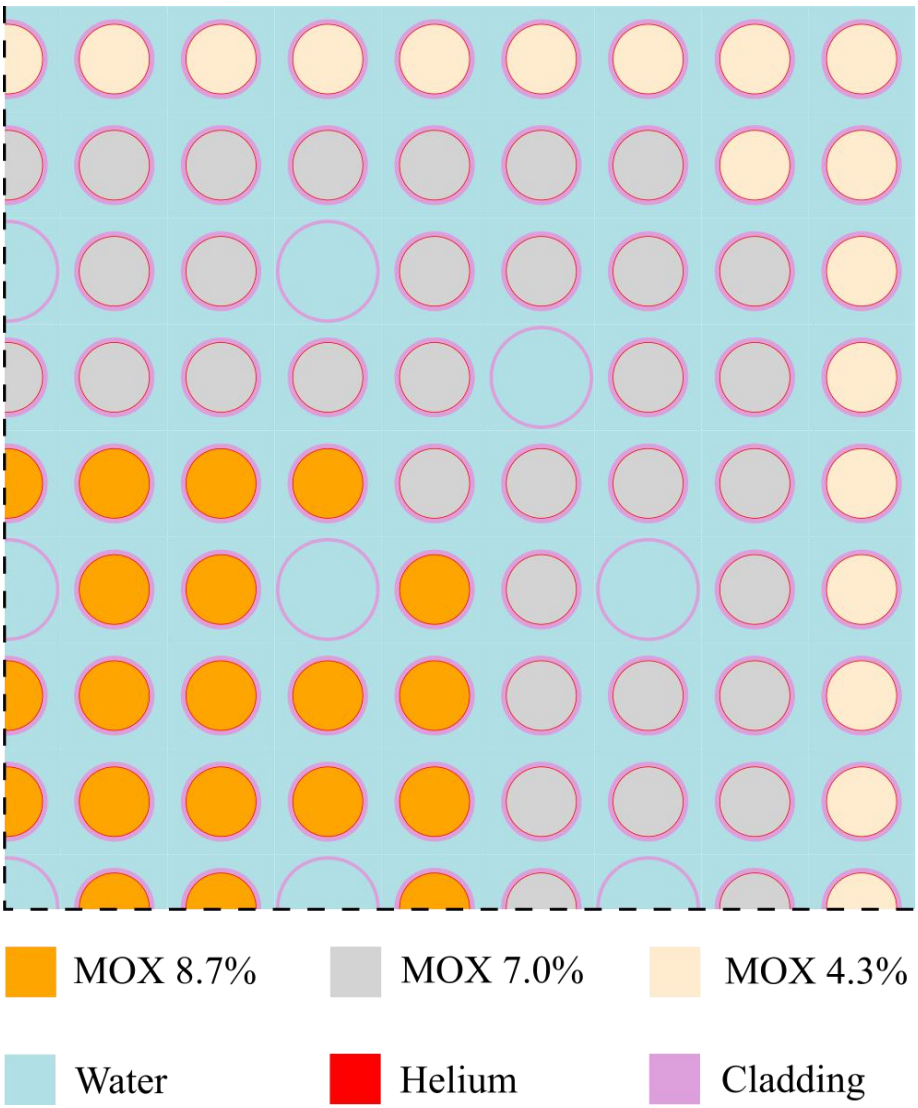

Figure 7. Material map of the KAIST1A MOX assembly (quarter symmetry)

The cold zero state with the temperature of all the materials equal to 300 K and without boric acid in the moderator was chosen for the simulations in the current study. The details of the material compositions of the fuel assembly used in calculations are presented in Table 3.

Table 3. Material's compositions used in the simulation of the KAIST 1A MOX assembly

Material	Material composition
MOX 4.3%: Pu-tot = 4.3 w/o	U235: 0.225 w/o Pu-tot: Pu238/239/240/241/242/Am241 = 1.83/57.93/22.50/11.06/5.60/1.08 w/o density: 10.4 g/cm^3
MOX 7.0%: Pu-tot = 7.0 w/o	
MOX 8.7%: Pu-tot = 8.7 w/o	
Water	H_2O density: 1.0 g/cm^3 (corresponds to the

	temperature 300K according to [20])
Helium	He (320psig/700 °K)
Cladding	Zircaloy (Zr-97.91%, Sn-1.59%, Fe-0.5%) density : 6.44 g/cm^3

4. Results and Discussions

In the current chapter, the results of the simulations are presented. The results of the simulations of the developed transport solver were compared with the reference Monte Carlo simulations. The reference solution for each benchmark problem were obtained using OpenMC code [21]. OpenMC is the open source Monte Carlo code developed at MIT. It is general purpose Monte Carlo code with the capability to simulate both eigenvalue and fixed source problems. For this study OpenMC code was used to simulate the problem with the given multigroup cross section sets.

4.1. Choice of the coupling parameters

The results of the simulations obtained using CCCP method depends on the spatial discretisation used for coupling of the currents on the cell's interfaces. In the current version of the solver, each side of the cell is discretised on the set of the segments; azimuthal and polar angles are subdivided on the set of the sectors. In order to choose an appropriate segment-angle discretisation of the test problems presented in the current study, a short sensitivity study was performed. The geometries of the test problem for the sensitivity study are shown in Figure 8.

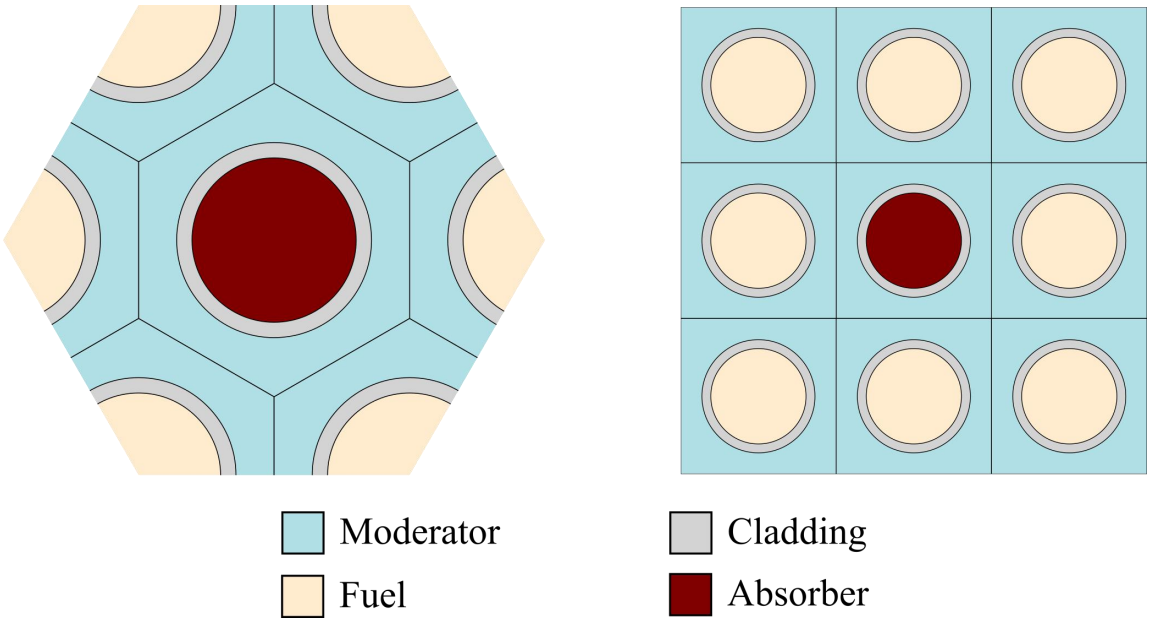

Figure 8. Material maps of the hexagonal (left) and square (right) supercells used for the sensitivity study

The cross sections of the materials are presented in Table 4.

Table 4. Cross sections of the materials used for the sensitivity study

Cross sections	Material			
	Fuel	Absorber	Cladding	Moderator
Σ_t,cm^{-1}	0.4082348	1	0.2662970	0.5919169
Σ_s,cm^{-1}	0.3371570	0.2997832	0.2644762	0.5896743
$\nu\Sigma_f$,cm^{-1}	0.1060497	0	0	0

The geometry was chosen to model highly heterogeneous structure with a strong neutron absorber placed in the centres of the supercells with reflective boundary conditions used for both supercells. Such an arrangement of the materials creates very high gradient of the flux which is challenging for the transport solver and requires the detailed discretisation of the space and angle variables to correctly reproduce the neutron currents on the cell's edges.

The results of the calculations are presented in Figure 9 and Figure 10.

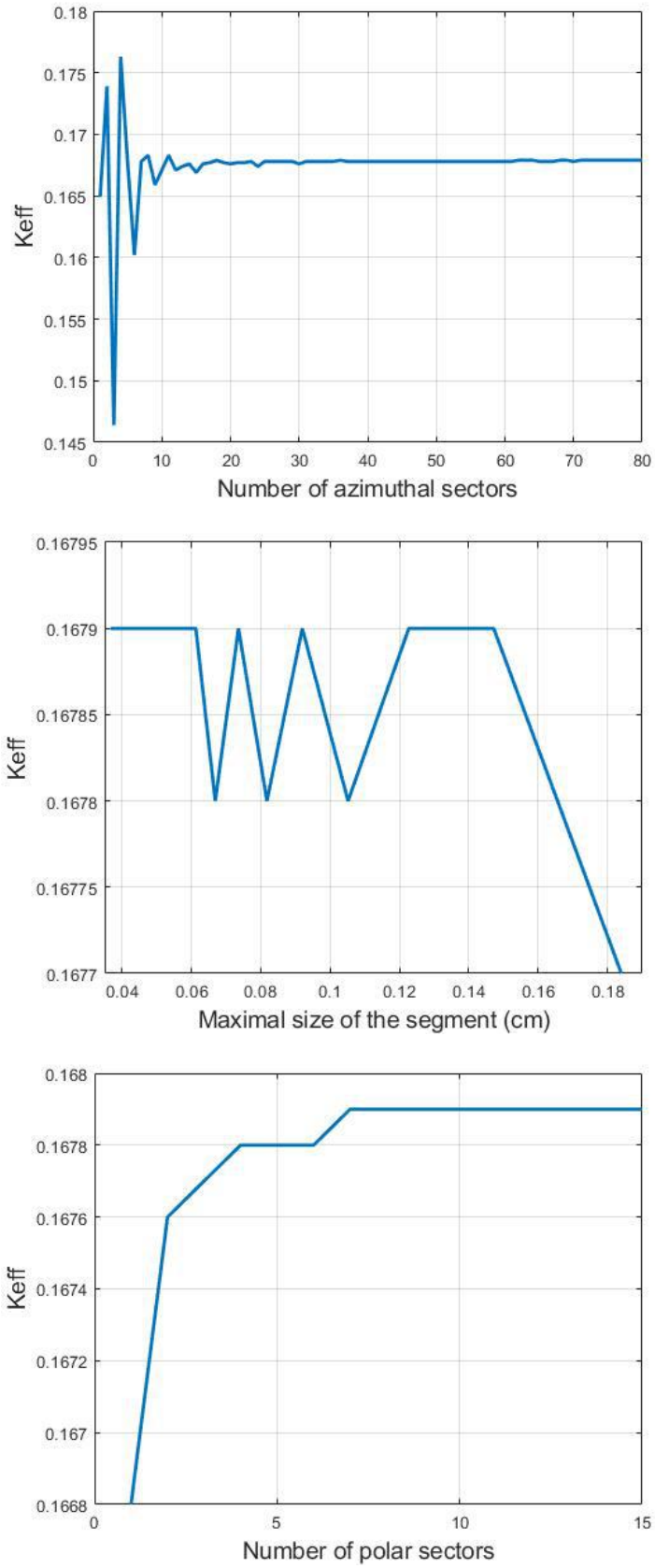

Figure 9. Dependency of the effective multiplication factor on number of azimuthal sectors (top), maximal size of the segment (middle) and number of polar sectors (bottom) for the square supercell

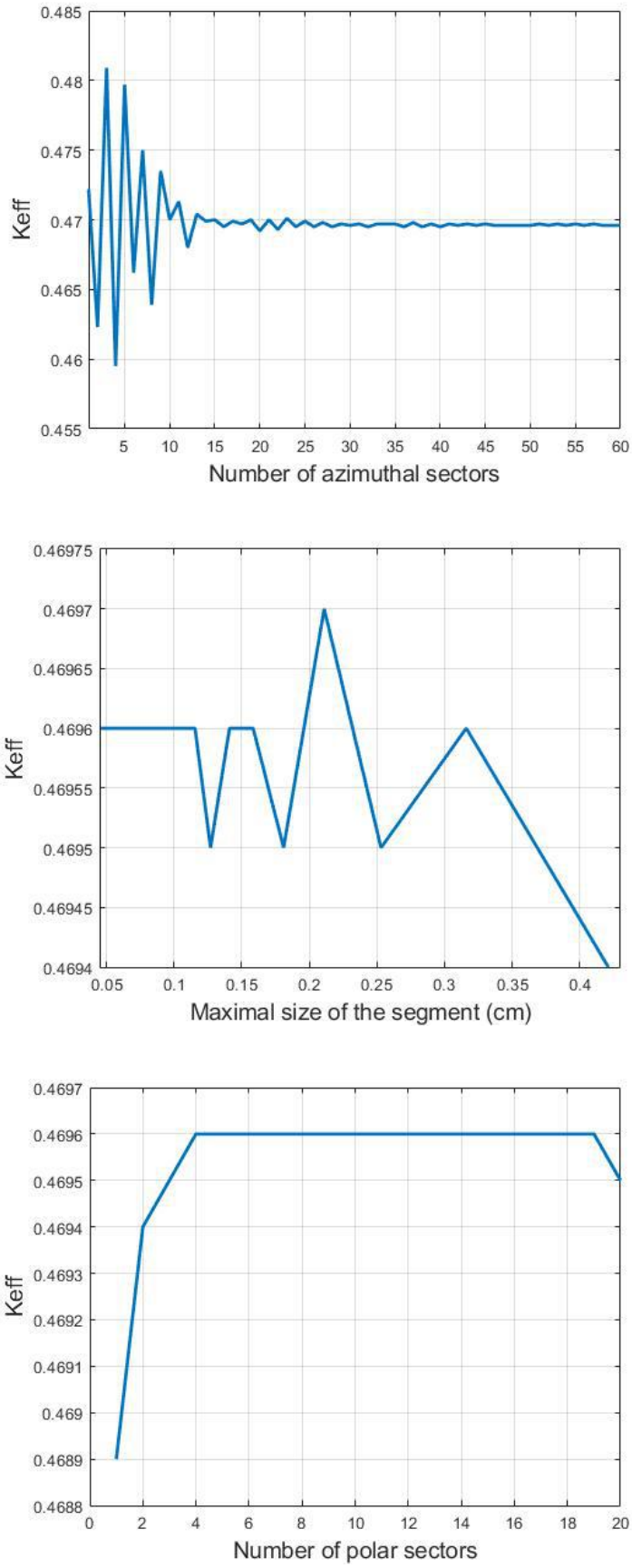

Figure 10. Dependency of the effective multiplication factor on number of azimuthal sectors (top), maximal size of segment (middle) and number of polar sectors (bottom) for the hexagonal supercell

As can be seen from the results of the asymptotic analysis, the effective multiplication factors tends to an asymptotic value as number of azimuthal angles N_φ, number of polar sectors N_θ increase and maximal size of the segment d_{seg} decreases. Asymptotic behaviour for the hexagonal supercell is achieved for the approximately $N_\varphi = 71$ azimuthal sectors, $d_{seg} = 0.0613$ cm size of the segment and $N_\theta = 7$ polar sectors; For the square assembly asymptotic behaviour is achieved for the $N_\varphi = 58$, $d_{seg} = 0.116$ and $N_\theta = 4$. In order to check the correctness of the chosen parameters, the comparison of the effective multiplication factors for the hexagonal and square MOX assemblies (see Chapter 3.2 and Chapter 3.3) with optimal (defined above) and fine ($N_\varphi = 160$, $d_{seg} = 0.04$, $N_\theta = 10$) coupling parameters were performed. The observed difference between eigenvalues was less than 20 pcm both for hexagonal ($k_{fine} = 1.20881$ and $k_{optimal} = 1.20898$) and square ($k_{fine} = 1.18669$ and $k_{optimal} = 1.18686$) assemblies. Therefore, the optimal sets of the coupling parameters were chosen for the calculations of the further hexagonal and square benchmark problems. Finally, we would like to note that this analysis is not a comprehensive asymptotic study since a substantial amount of the parameters (such as number of groups, lattice pitch, moderator density, etc.) were not considered here. Involvement of the other parameters in analysis would require additional broad investigations which are out of scope of the current study.

4.2. Results of the one group fixed source simulations

A one group fixed source problem was calculated both for the hexagonal and square geometries. The relative statistical difference of the reference OpenMC solution did not exceed 0.2% for the fluxes with 99.7% confidence interval ($\pm 3\sigma$) for both geometries. Hexagonal and square test problems were calculated for 0th, 1st and 2nd orders of the polynomials used for the spatial flux expansion. The relative absolute errors of the transport solver in comparison to the reference OpenMC solution for hexagonal and square assemblies are presented in Figure 11 – Figure 16. As it was expected, the maximal error for the flat flux approximation (P0) is observed in the central cell surrounded by the strong absorbers. The errors for the flat flux approximation are quite high both for hexagonal and square assemblies. The influence of the order of polynomials used for the flux expansion has a high impact on the results. Even the first order of the polynomials applied in the hexagonal assembly allow for the reduction of the maximal error from 18.2% to 1.4% and from 13.7% to 2.9% in the central regions. The same order of the improvements is observed for the square assemblies. Further increasing of the polynomials order brings the errors to the level below 1%. For the averaged fluxes the situation is similar both for hexagonal and square assemblies.

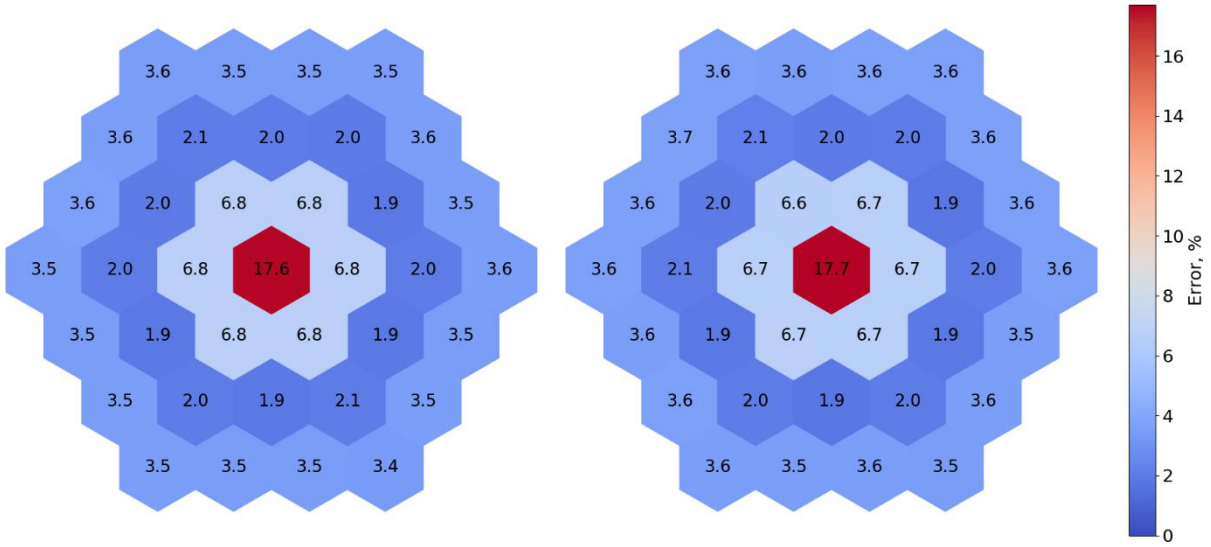

Figure 11. Errors in the fuel (left) and average (right) fluxes for the hexagonal fixed source problem (0-th order of flux expansion)

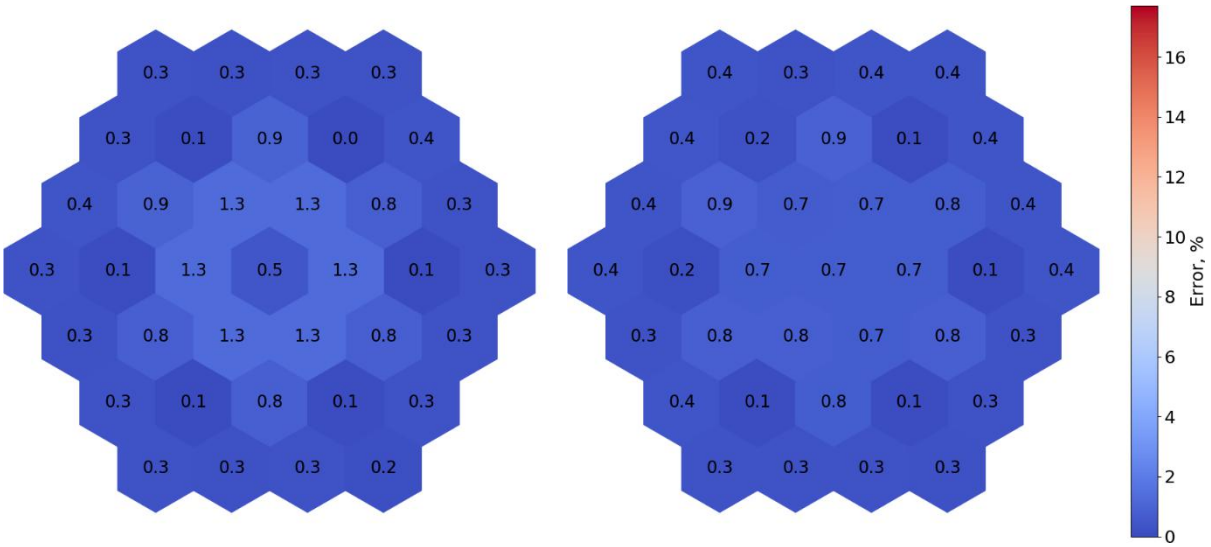

Figure 12. Errors in the fuel (left) and average (right) fluxes for the hexagonal fixed source problem (1-st order of flux expansion)

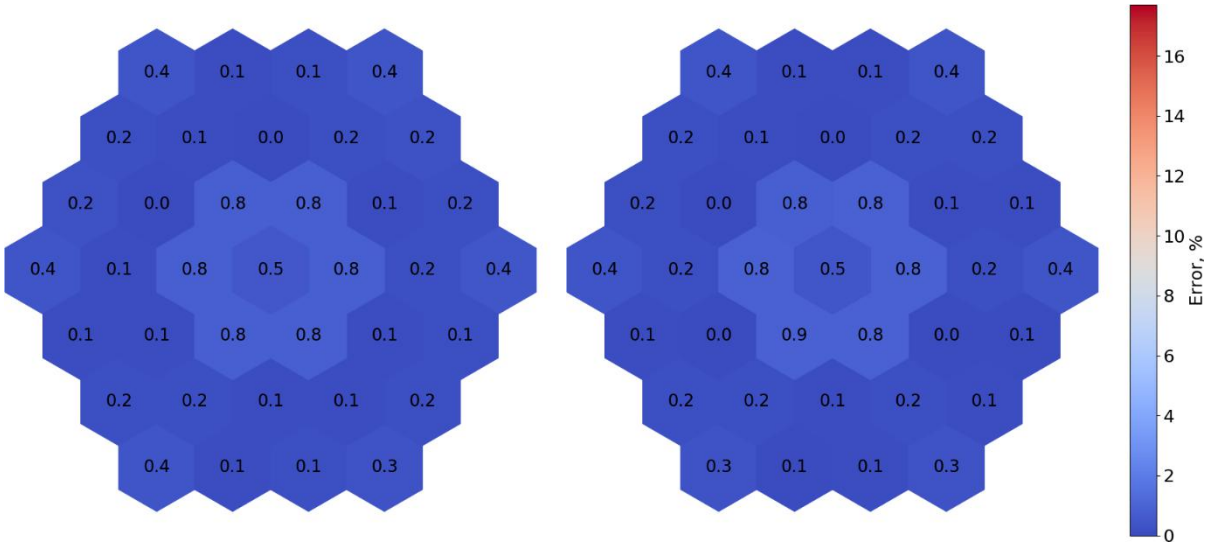

Figure 13. Errors in the fuel (left) and average (right) fluxes for the hexagonal fixed source problem (2-nd order of flux expansion)

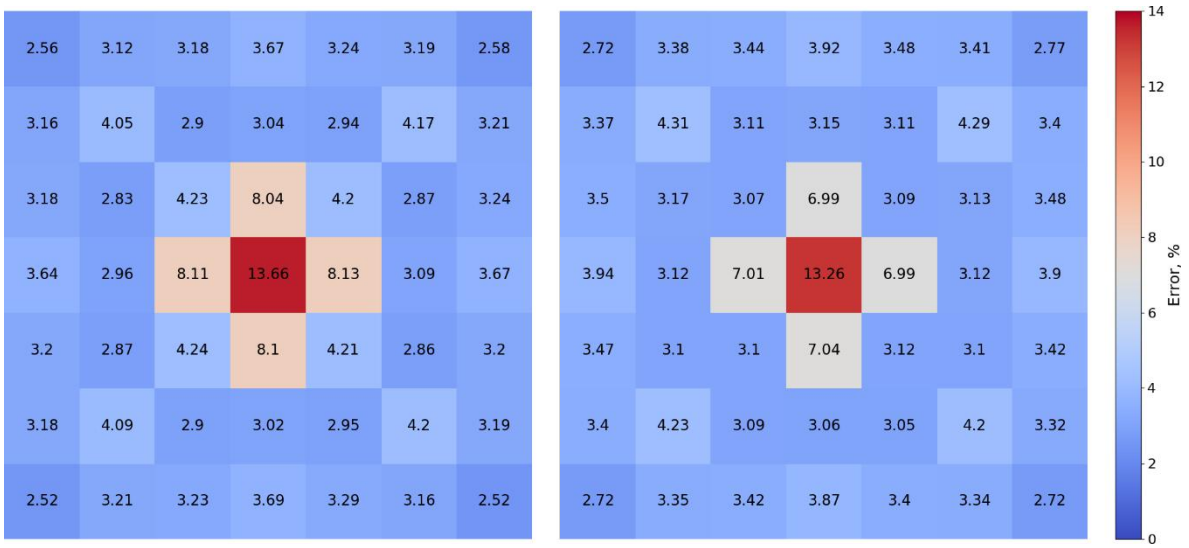

Figure 14. Errors in the fuel (left) and average (right) fluxes for the square fixed source problem (0-th order of flux expansion)

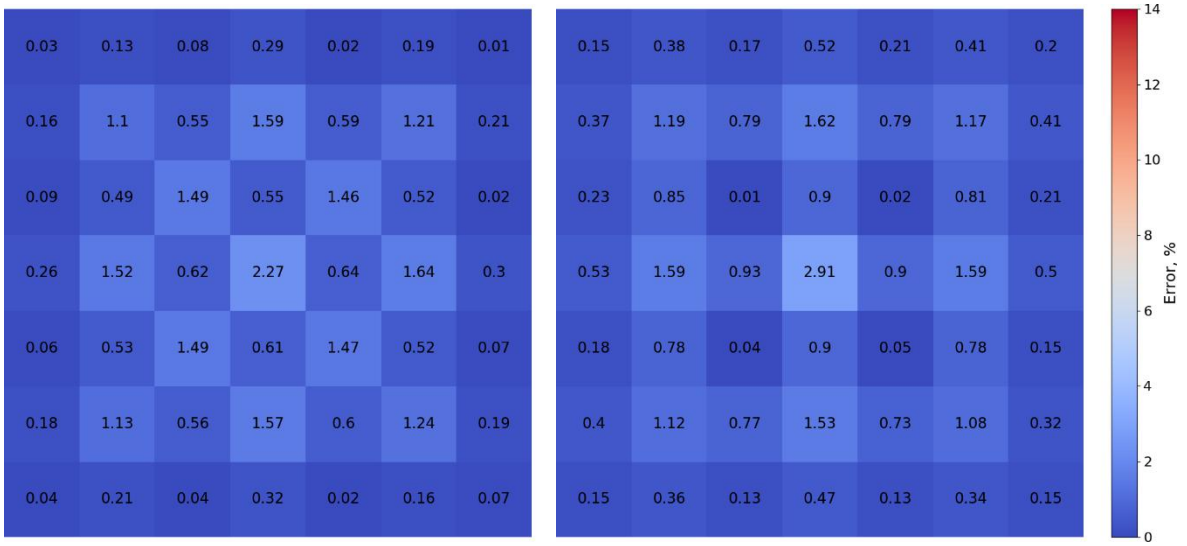

Figure 15. Errors in the fuel (left) and average (right) fluxes for the square fixed source problem (1-st order of flux expansion)

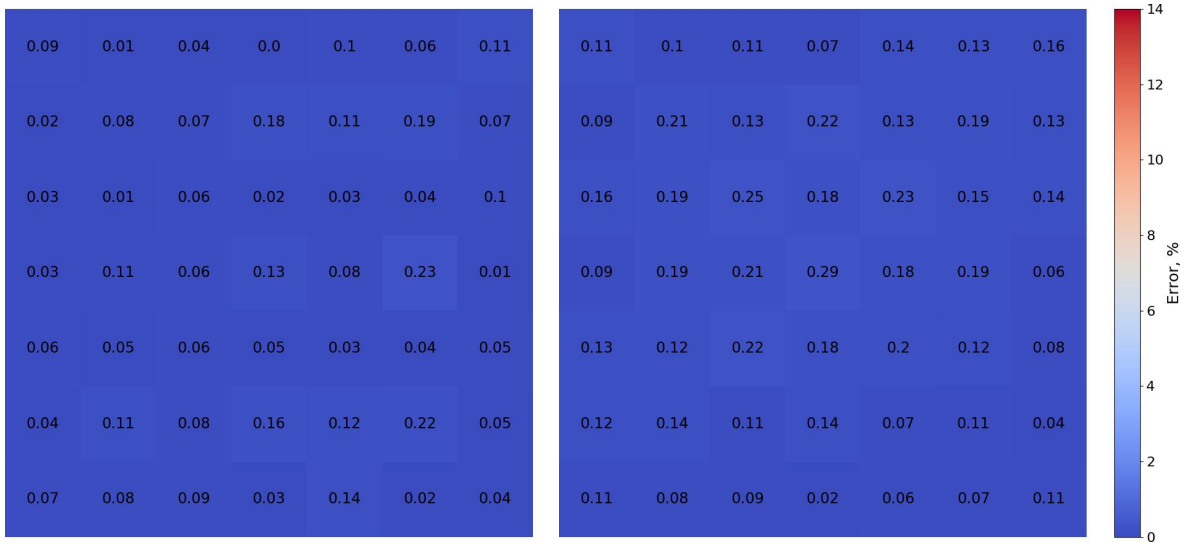

Figure 16. Errors in the fuel (left) and average (right) fluxes for the square fixed source problem (2-nd order of flux expansion)

4.3. *Results of the hexagonal C5G7 MOX assembly simulations*

The results of the simulations of the square C5G7 MOX assembly are summarised in Table 5 and Figure 17.

Table 5. Effective multiplication factors, maximal and root mean square (RMS) errors for the single C5G7 MOX assembly

Order of flux expansion	k_{eff}	Δk_{eff}, pcm	Absolute maximal error, %	RMS error, %
P_0	1.20898	249	5.05	2.01
P_1	1.20742	93	0.39	0.17
P_2	1.20705	56	0.20	0.07

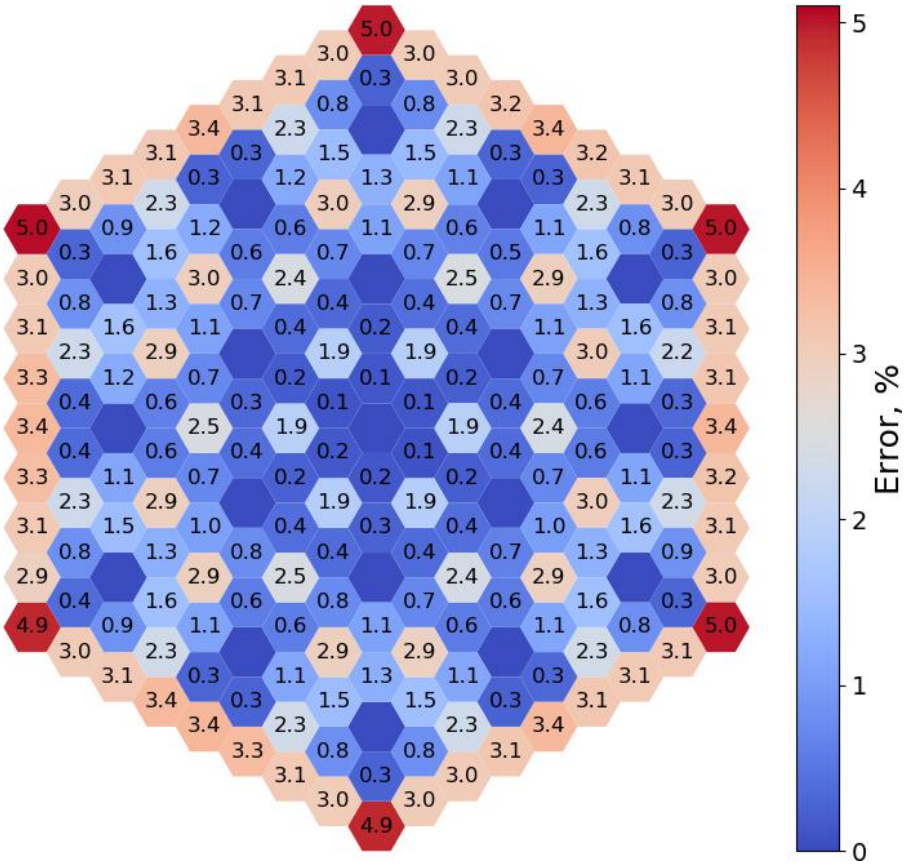

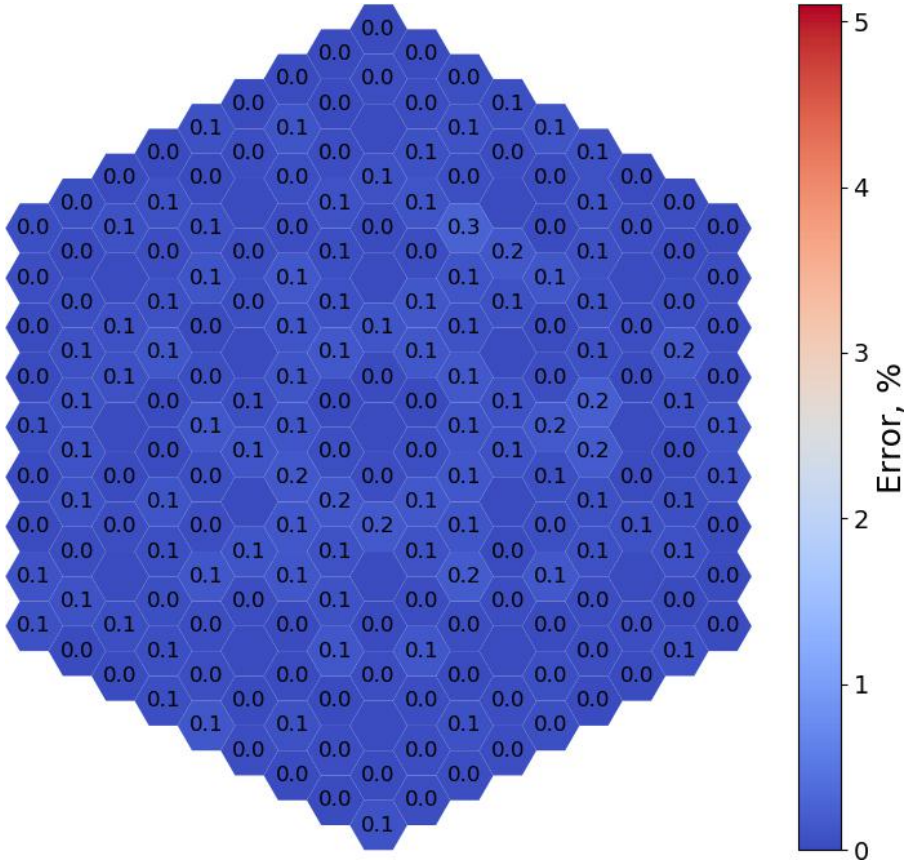

Figure 17. Absolute relative errors for P0 (top) and P2 (bottom) orders of flux expansion

Overall good agreement with the reference Monte Carlo results is observed. The difference in effective multiplication factor, maximal and root mean square errors decrease monotonically with increasing of the order of the polynomials used for the flux expansion. Maximal error decreases from approximately 5% to 0.2% while root mean square error decreases from 2.01% for P_0 approximation to 0.07% for the second order of the polynomials. The discrepancies in the fission rates and eigenvalue have, in our view, two main contributors of the errors. First, it seems to be that even the second order of the polynomials is still not enough to reproduce the shape of the flux completely. Therefore, we expect that the higher orders of the polynomials can lead to better results. Second source of the errors is still not completely converged Monte Carlo solution (see non-symmetry of the observed errors in Figure 17). Therefore, for a comprehensive comparison, the statistical error of the Monte Carlo simulations should be further reduced.

4.4. Results of the KAIST 1A MOX assembly simulations

The modelling of the KAIST 1A MOX fuel assembly consisted of two stages. On the first stage, two sets of the multigroup cross sections were prepared using the OpenMC code running in continuous energy mode with ENDFB-VII.1 library. The neutron cross sections were collapsed into

the 2-groups and 8 groups. The group boundaries are presented in Table 6 and corresponds to the CASMO-2 and CASMO-8 energy group structures as they are available in the OpenMC code [22].

Table 6. Group energy structures

Group number (2 groups)	Group number (8 groups)	Lower energy bound, eV
1	1	$8.21 \cdot 10^5$
	2	$5.53 \cdot 10^3$
	3	4.0
	4	0.625
2	5	0.28
	6	0.14
	7	0.058
	8	0.0

Generated cross sections sets were used for the few-groups simulations using CCCPO neutron transport solver. Multiplication factors and fission reaction rates were calculated both in 8 groups and in 2 groups using different orders of the flux expansion. The same cross sections were used for the multigroup simulations using OpenMC code. The eigenvalue obtained using continuous energy Monte Carlo simulation and discrepancies with the CCCPO solver and multigroup Monte Carlo calculations are presented in Table 7.

Table 7. Discrepancies between eigenvalues calculated using continuous energy Monte Carlo and multigroup methods

Number of groups	OpenMC CE, eigenvalue	Discrepancies with the OpenMC CE, pcm			
		OpenMC MG	CCCPO P_0	CCCPO P_1	CCCPO P_2
2	1.31445	-159	-28	-49	-80
8		-367	-274	-302	-304

The results presented in Table 7 demonstrate that the discrepancies in the infinite multiplication factors calculated using developed transport less than 100 pcm for the 2 groups and

around 300 pcm for the 8 groups. Surprisingly, increasing of the group number used for simulation does not lead to the improving of the effective multiplication factor. It contradicts the results obtained in the previous chapters where increase of the polynomial order led to the better results. Another interesting observation is that the increasing of the polynomial order increases the discrepancies in the eigenvalues. Therefore, the results should be discussed in more details.

In order to clarify the situation, the fission reaction rates calculated using neutron transport solver, continuous energy OpenMC and multi group OpenMC were compared. Results of the comparison are presented in Table 8 and Figure 18 – Figure 20.

Table 8. Discrepancies in fission reaction rates between continuous energy OpenMC and multi group simulations

Number of groups	Absolute maximal error, %				RMS, %			
	P_0	P_1	P_2	OpenMC MG	P_0	P_1	P_2	OpenMC MG
2	4.8	4.3	4.5	4.3	1.9	1.8	1.7	1.7
8	1.9	1.9	2.0	2.1	0.7	0.7	0.9	0.9

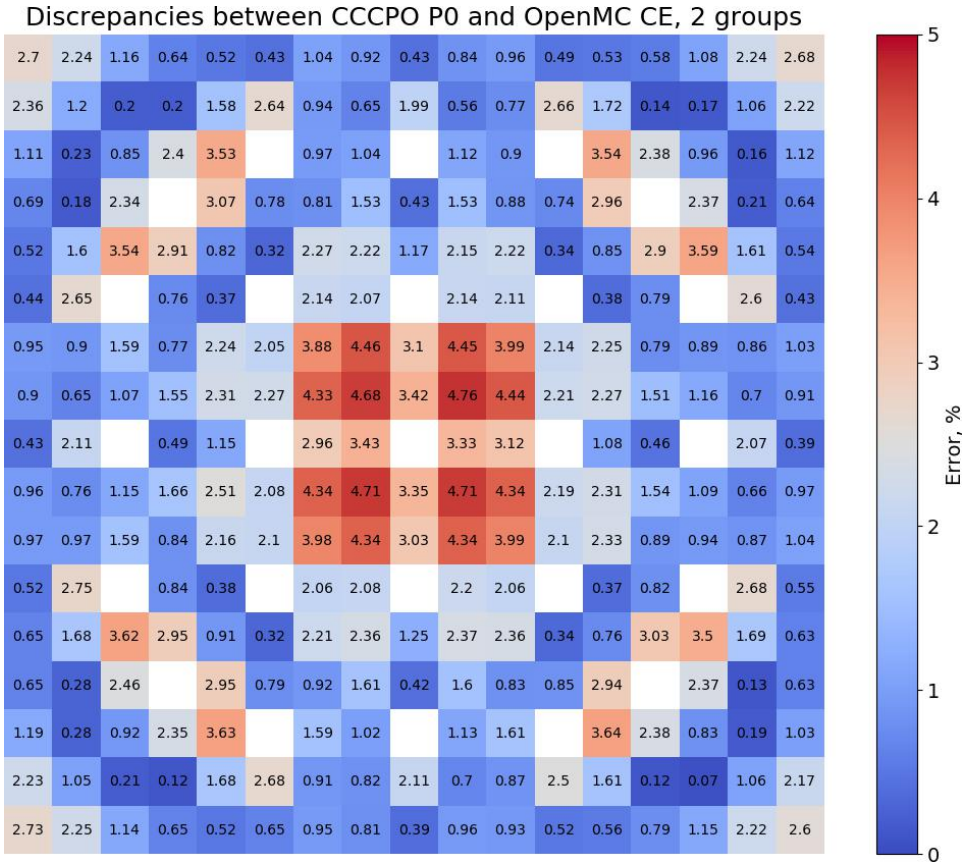

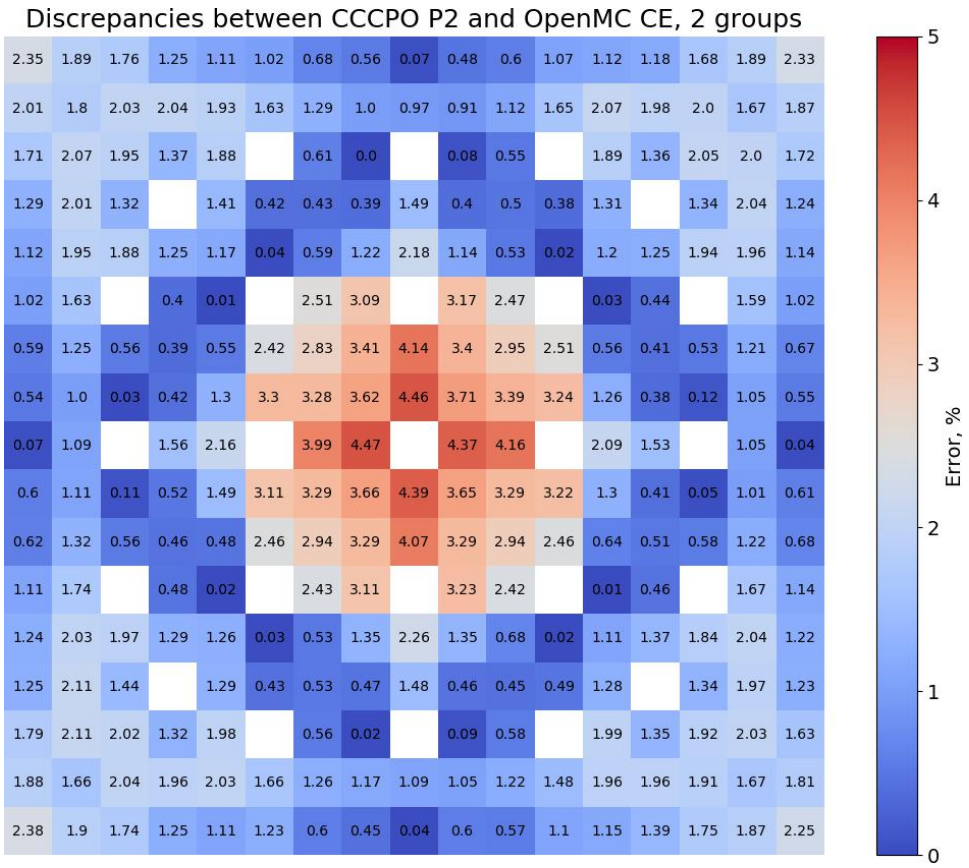

Figure 18. Discrepancies in fission rates between continuous energy OpenMC and neutron transport solver (2 groups) with zero (left) and second (right) orders of flux expansions

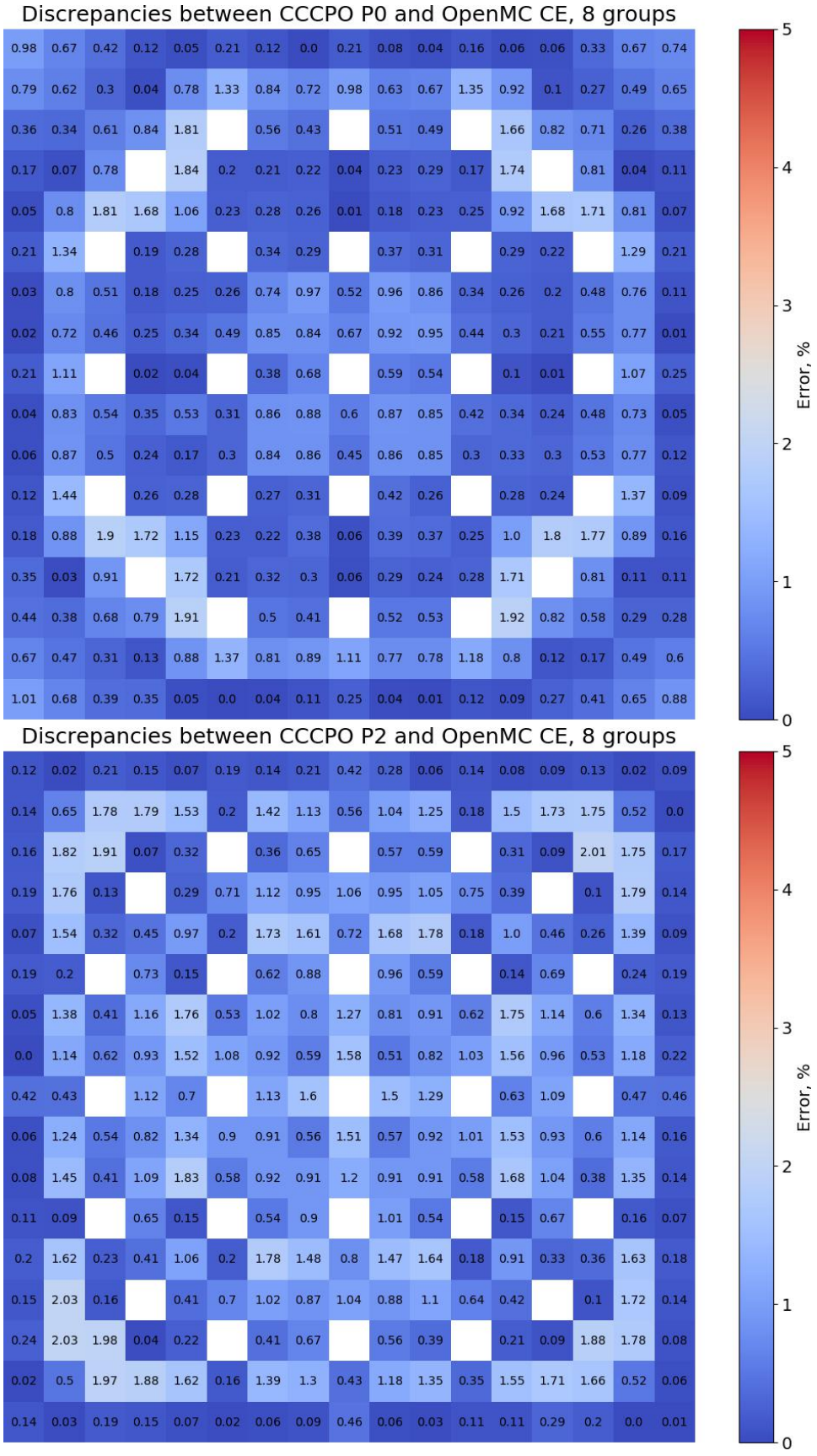

Figure 19. Discrepancies in fission reaction rates between continuous energy OpenMC and neutron transport solver (8 groups) with zero (top) and second (bottom) orders of flux expansions

As it is observed from Table 8, both maximal and root mean square errors are higher for the case of the two groups despite the fact that the effective multiplication factors calculated using 2 groups are closer to the reference continuous energy eigenvalue. This contradiction can be explained, in our view, by the error cancellation observed for the two group structure. In the opposite case, the errors in the fission reaction rates would also be closer to the continuous energy OpenMC results than the results calculated using 8 groups.

Application of the higher order of the polynomials for the flux expansion does not improve the results in comparison to the flat flux approximation (compared to the continuous energy Monte Carlo simulations). The errors stay almost on the same level or even become slightly higher. It contradicts results obtained in the previous chapters where application of the higher order of the flux expansion improved the results. In order to clarify the situation, the distribution of the discrepancies in fission rates between multi group and continuous energy OpenMC simulations was created (see Figure 20).

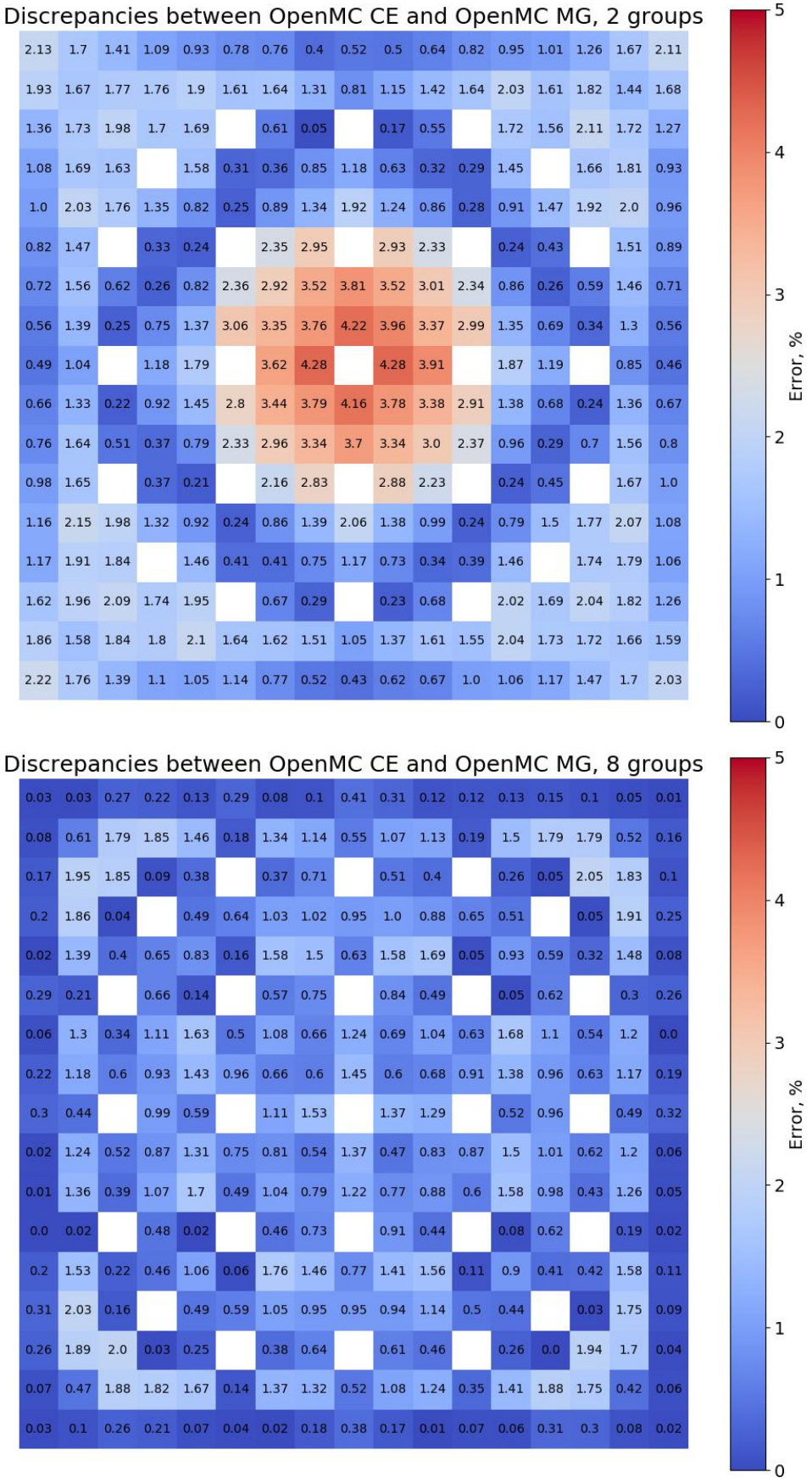

Figure 20. Discrepancies in fission reaction rates between continuous energy OpenMC and multi group OpenMC with 2 groups (top) and 8 groups (bottom)

As it is observed from Figure 18, the error distribution (as well as maximal and root mean square error, see Table 8) is very similar to the error distribution observed for the second order of flux expansion in Figure 19 (2 groups) and Figure 20 (8 groups). The situation becomes clearer when the fission reaction rates obtained using neutron transport solver and multi group Monte Carlo are compared (see Figure 21).

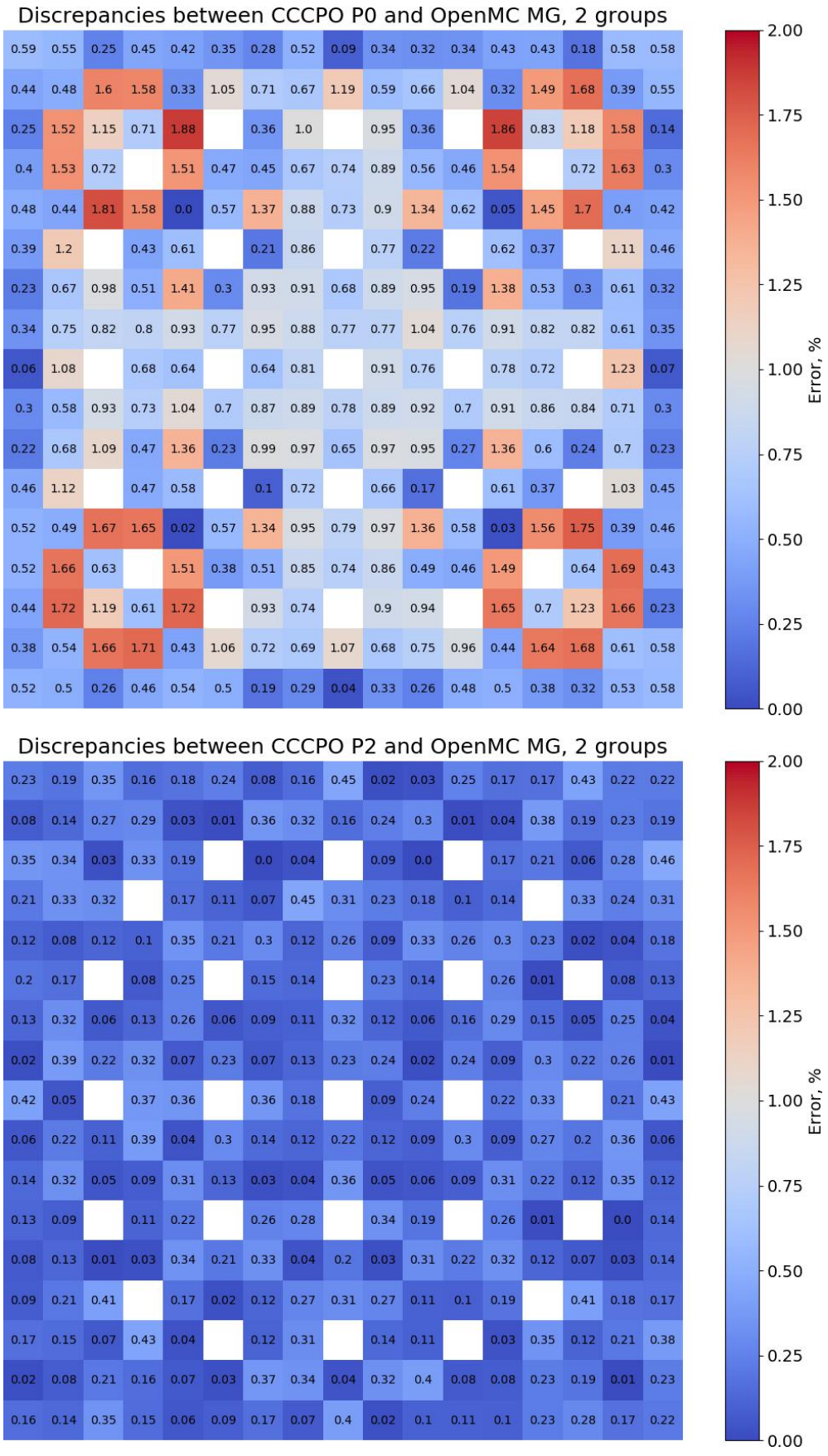

Figure 21. Discrepancies in fission reaction rates between multi group OpenMC and neutron transport solver (2 groups) with zero (top) and second (bottom) orders of flux expansions

As it can be seen from Figure 21 the discrepancies in the fission reaction rates between multi group OpenMC and neutron transport solver decrease significantly when the second order of the fluxes are applied. Maximal difference decreases from approximately 1.9% to 0.5% while root mean square difference decreases from 0.8% to 0.2%. These results coincide very well with the results observed in the previous chapters.

Summarising the results of the KAIST 1A MOX Assembly benchmark, we can conclude that the main source of the observed error in the fission reaction rates and eigenvalues is not the quality of the neutron transport solver but the homogenisation and collapsing technique used for the few group cross section generation. The results obtained by the neutron transport solver are very close to the results obtained by the multi group Monte Carlo method. The bias between the eigenvalues and reaction rates computed using multi-group method and continuous energy method can be reduced if the further higher order approximations are applied. It can be (but not limited to) application of the higher order of the neutron scattering, cross-sections dependent on angle, higher number of energy groups.

5. Visualisation

Further verification of the developed neutron transport solver was performed with the help of visualisation techniques. The neutron flux within a 3 by 3 supercell with the strong absorber in the center (see Figure 22) was calculated using OpenMC code and the neutron transport solver.

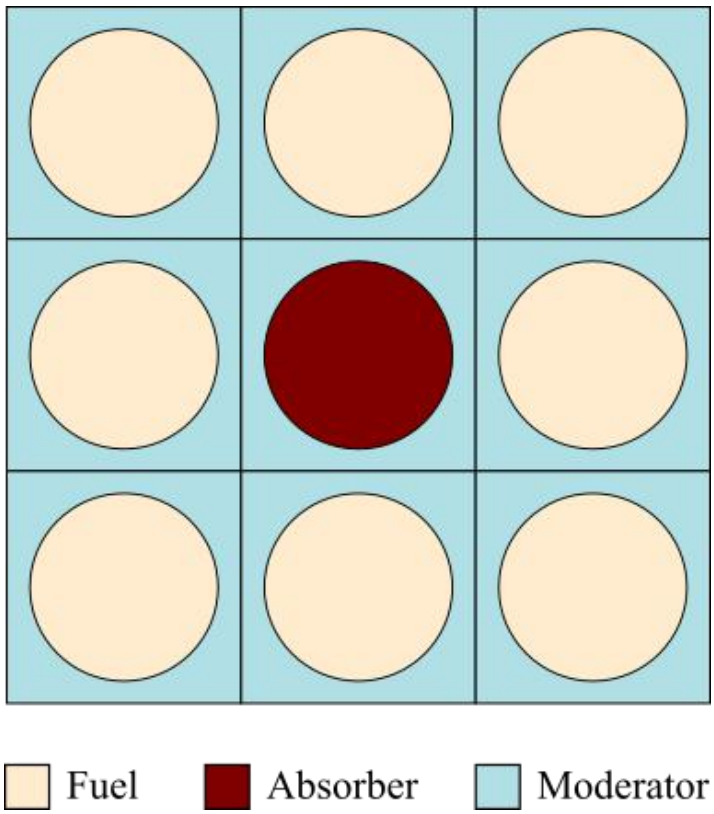

Figure 22. Material map of the supercell used for the visualisation

In order to obtain the neutron flux calculated by the Monte Carlo method, a very fine tally mesh (900x900) was used. The same mesh was used for the deterministic simulations. However, in contrast to the Monte Carlo methodology, the neutron flux within each mesh point was reconstructed using the orthogonal polynomials and values of the spatial moments of the neutron flux. The neutron flux was calculated for the thermal and fast groups. The results of the visualisation are presented in Figure 23 and Figure 24.

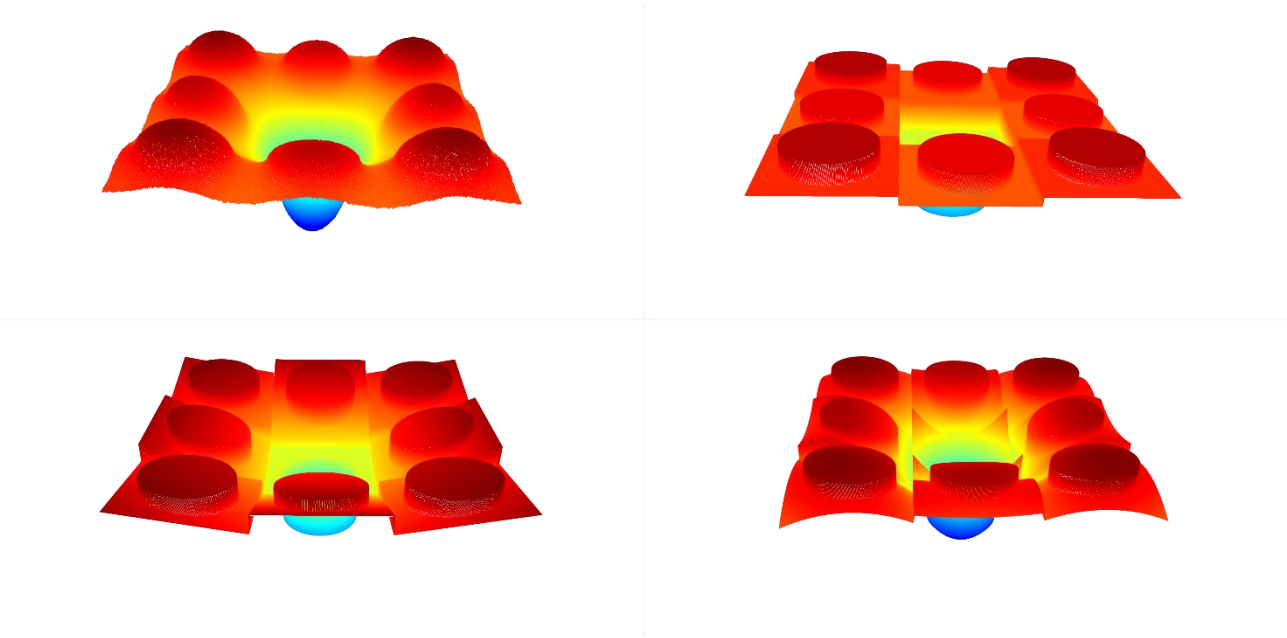

Figure 23. Visualisation of the fast flux within the supercell calculated by Monte Carlo (upper left), P0 CCPO (upper right), P1 CCCPO (lower left) and P2 CCCPO (lower right)

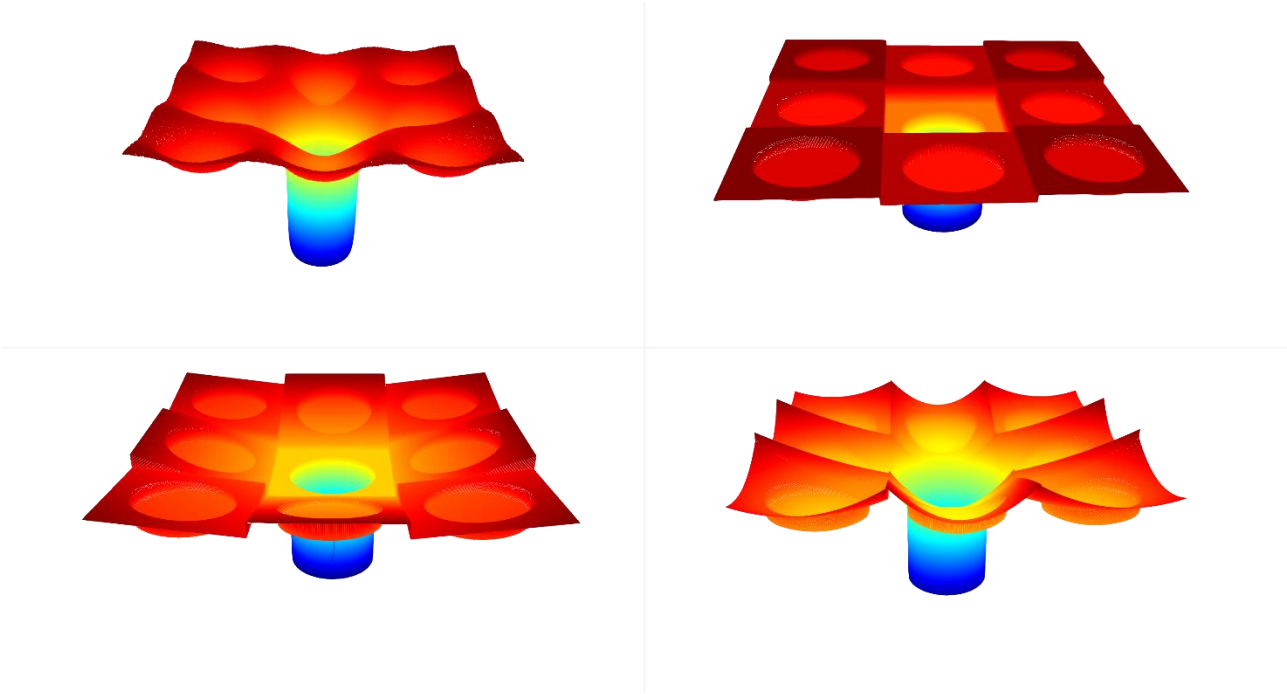

Figure 24. Visualisation of the thermal flux within the supercell calculated by Monte Carlo (upper left), P0 CCPO (upper right), P1 CCCPO (lower left) and P2 CCCPO (lower right)

Results of the calculations were visualised using ParaView application [23]. The shape of the flux behaves as expected for the problem under consideration. In the fast group the peak neutron flux occurs in the fuel regions with the cavity in the center of the supercell where neutrons are absorbed due to the presence of the absorber. The situation is different for the thermal energy group where neutron flux is higher in the moderator regions due to the moderation of the neutrons with the

small cavities in the fuel regions and deep cavity in the central part once more due to the strong absorption of the neutrons.

The results of the visualisation clearly demonstrate improvements in the flux shape as the order of the polynomials, used for the flux expansion increases. The shape of the flux changes from the flat planes for the 0-th order of the polynomials to the second order surfaces for the 2-nd order expansion of the flux. The first order of the flux expansion is somewhere between 0-th and 2-nd orders with the inclined planes in the fuel cells and flat planes in the central part. Despite the visible improvements in the flux shape for the second order of the polynomials, the shape of the flux is still quite far from the smooth reference shape of the flux. It demonstrates, in our view, that 2-nd order of the flux is still not enough for precise approximation of the flux shape. Therefore, higher levels of the polynomials are required to reproduce the flux shape more accurately.

6. Analysis of the transport solver's performance

The expansion of the flux by orthogonal polynomials improves the accuracy of the neutron transport simulations significantly in comparison with the conventional flat flux approximation. However, it should be noted that the computational time increases when a higher order of the polynomials are applied for the flux expansion. In order to estimate the real benefits of the higher order flux expansion, a comparison of the simulation time with the flat flux approximation should be performed. Therefore, in the current chapter, a preliminary analysis of the performance of the developed neutron transport solver for different orders of flux expansion is undertaken. The fixed source test problem (square assembly) defined in chapter 3.2, was used for this analysis. As has already been mentioned, a higher of calculation regions will lead to a more accurate result, when using the flat flux approximation. However, by increasing the number of calculation regions this leads to longer simulation times. To understand the additional simulation times required when increasing the accuracy, the next study investigates the impact on the simulation time when using a variety of orders of the flux expansion and numbers of the simulation regions. The outermost (moderator) regions of the fuel and absorber cells in the square assembly were subdivided into the set of the concentric subregions as it is shown in Figure 25 to provide the additional regions for the study.

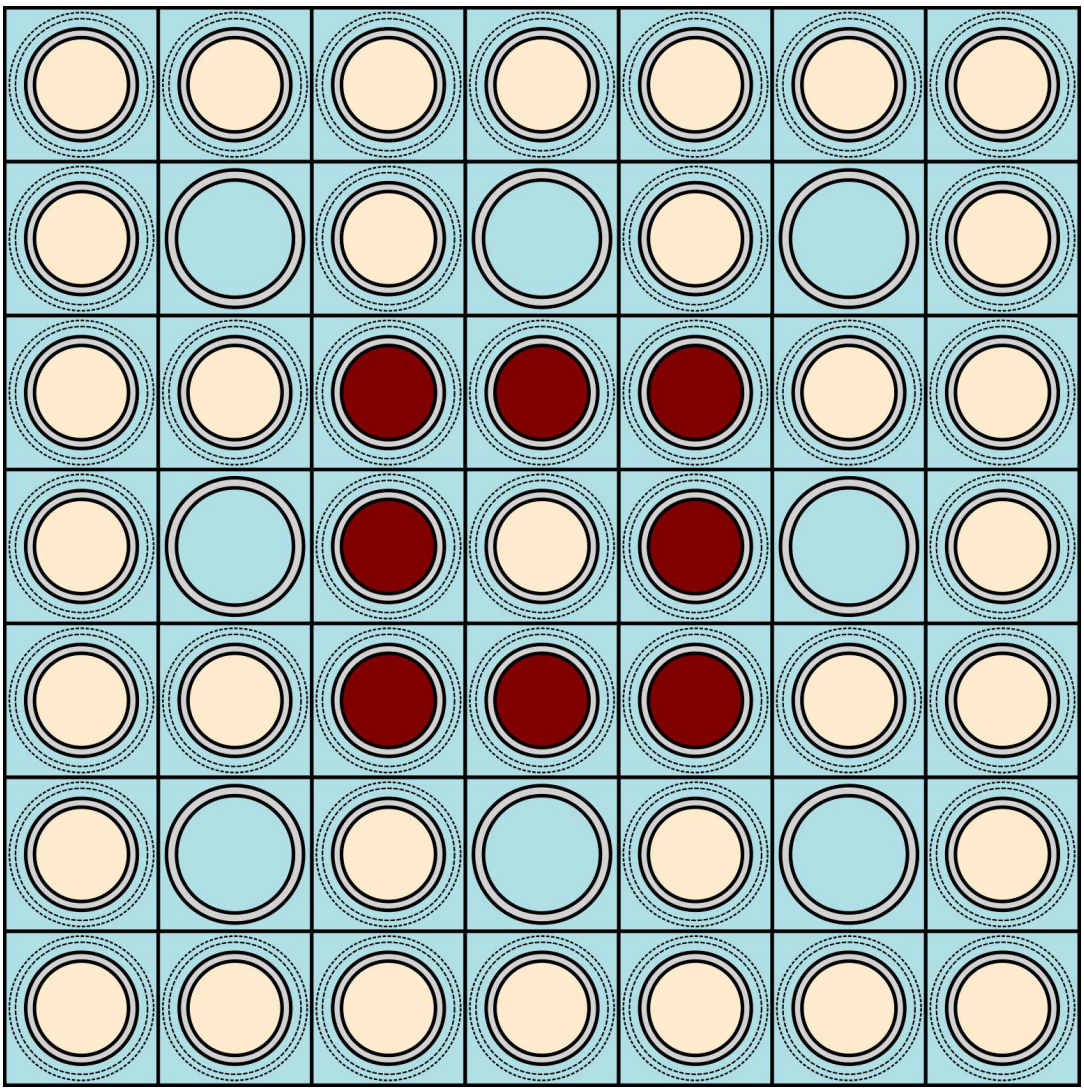

Figure 25. Subdivision of the moderator region on subregions (dotted lines)

The results of the numerical experiments are summarised in Table 9. In the first column of Table 9 the number of the subregions in the moderator are given. In the second and third columns ratios of the computation times between P_1 and P_0 ($\frac{t_{P_0}}{t_{P_1}}$) as well as between P_2 and P_0 ($\frac{t_{P_0}}{t_{P_2}}$) are given.

Table 9. Results of the simulation time's comparison

Number of subregions	$\frac{t_{P_0}}{t_{P_1}}$	$\frac{t_{P_0}}{t_{P_2}}$
1	0.61	0.32
2	0.70	0.37
3	0.82	0.44

4	0.97	0.52
5	1.21	0.65
6	1.49	0.80
7	1.88	1.00
8	2.21	1.18
9	2.40	1.28
10	2.90	1.55
11	3.45	1.84
12	4.22	2.25

It is observed from Table 9 that the computational time for the flat flux approximation without subdivision of the moderator zone is more computationally expensive in comparison with both P_0- and P_2-approximations. However, by increasing the number of subregions this leads to higher simulation times of the flat flux approximation. As a result, the P_1 approximation becomes more efficient than the flat flux approximation with five sub regions, and the P_2 approximation becomes comparable with the flat flux approximations with seven subregions. Finally, it should be noted that the accuracy of the simulations is not presented here since it is not enough to subdivide the outermost region only to obtain accurate results for the flat source approximation. It is common practice to add straight lines connecting, for example, vertices of the cell into the subdivision scheme as it is shown in Figure 26.

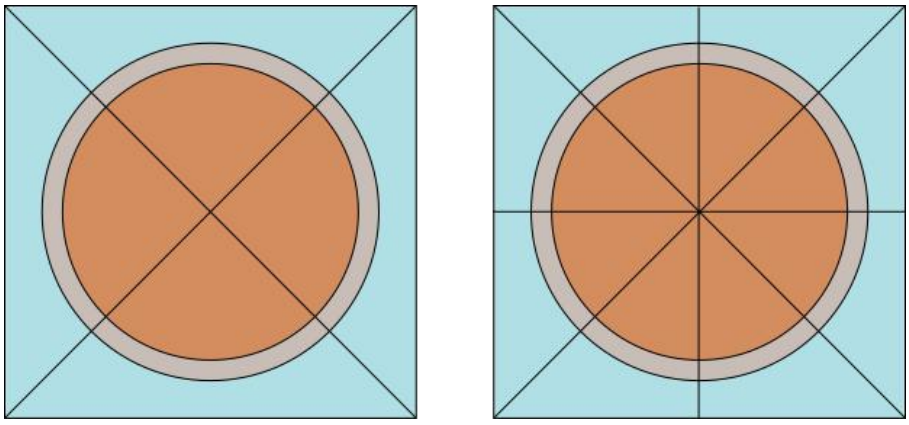

Figure 26. Example of the cell's subdivision on 12 (left) and 24 (right) flat source regions

The typical scheme of the square cell's subdivision involves at least 12 subregions for the cell consisting of moderator, cladding and fuel regions. This type of subdivision was not tested due to the limitations of the current version of the solver. Nevertheless, we expect that the performance of

the flat-flux approximation with the discretised regions will be comparable with the results for 12 subregions presented in Table 9.

7. Conclusions

In this study, the developed neutron transport solver utilising current coupling collision probability method with orthogonal flux expansion was tested and verified on the set of different benchmark problems. Application of the orthogonal polynomials for the representation of the sources/fluxes within calculation regions allows to overcome one of the drawbacks of the traditional collision probability method – poor representation of the spatial neutron source/flux distribution. The results of the deterministic simulations were compared with the reference Monte Carlo results. It was observed that the expansion of the flux by orthogonal polynomials allows us to avoid discretisation of the calculation regions while keeping the accuracy of the calculations on an acceptable level. Higher order of the fluxes reduces the error in the fission rates and neutron fluxes significantly. The results of the calculations demonstrate good agreement with the results of the Monte Carlo calculations. The comparison of the new method with the flat flux approximation demonstrates either an improved quality of the result for identical cell discretisation or reduced computational time to achieve an identical solution. The overall performance of the developed transport solver is acceptable from engineering point of view. Thus, in our view, it can be applied for the multiscale/multidimensional simulations. As a further step, the developed neutron transport solver will be integrated (coupled) with the nodal DYN3D code for further multiphysics/multidimensional study.

8. Acknowledgement

The authors would also like to acknowledge the support of the EPSRC through the funding of the EPSRC grant “Innovative LWR Simulation Tool for the Nuclear Renaissance in the UK” (EPSRC grant EP/R005850/1).

9. Bibliography

[1] P. K. Hutt, N. Gaines, M. McEllin, R. J. White, and M. J. Halsall, ‘The UK core performance code package’, *Nuclear Energy*, vol. 30, no. 5, pp. 291–298, 1991.

[2] U. Rohde *et al.*, ‘The reactor dynamics code DYN3D – models, validation and applications’, *Progress in Nuclear Energy*, vol. 89, pp. 170–190, 2016, doi: https://doi.org/10.1016/j.pnucene.2016.02.013.

[3] ‘Home | The Consortium for Advanced Simulation of Light Water Reactors’. https://www.casl.gov/ (accessed Nov. 14, 2019).

[4] B. Lindley *et al.*, 'Modelling and Simulation Activities in Support of the UK Nuclear R&D Programme on Digital Reactor Design', Volume 3: Nuclear Fuel and Material, Reactor Physics, and Transport Theory, Jul. 2018, doi: 10.1115/ICONE26-81090.
[5] B. Chanaron *et al.*, 'Advanced multi-physics simulation for reactor safety in the framework of the NURESAFE project', *Annals of Nuclear Energy*, vol. 84, pp. 166–177, Oct. 2015, doi: 10.1016/j.anucene.2014.12.013.
[6] B. Kochunas *et al.*, 'VERA Core Simulator Methodology for Pressurized Water Reactor Cycle Depletion', *Nuclear Science and Engineering*, vol. 185, no. 1, pp. 217–231, Jan. 2017, doi: 10.13182/NSE16-39.
[7] B. S. Collins, 'Multiscale Methods for Nuclear Reactor Analysis', PhD Thesis, The University of Michigan, 2011.
[8] K. Koebke and M. R. Wagner, 'The determination of the pin power distribution in a reactor core on the basis of nodal coarse mesh calculations', *Atomkernenergie*, vol. 30, no. 2, pp. 136–142, 1977.
[9] D. Litskevich, 'Development of an advanced neutron transport solver for zooming in DYN3D', Dissertation, RWTH Aachen University, Aachen, 2017.
[10] E. A. Villarino, R. J. J. Stamm'ler, A. A. Ferri, and J. J. Casal, 'HELIOS: Angularly Dependent Collision Probabilities', *Nuclear Science and Engineering*, vol. 112, no. 1, pp. 16–31, 1992, doi: 10.13182/NSE112-16.
[11] I. E. Rubin and N. M. Dneprovskaya, 'Heterogeneous calculation of hexagonal lattices by the method of passage probabilities', *Atomic Energy*, vol. 87, no. 5, pp. 791–797, Nov. 1999, doi: 10.1007/BF02673275.
[12] O. Safarzadeh, A. Minuchehr, and A. S. Shirani, 'Heterogeneous reactor core transport technique using response matrix and collision probability methods', *Annals of Nuclear Energy*, vol. 62, pp. 137–143, Dec. 2013, doi: 10.1016/j.anucene.2013.06.011.
[13] C. Wempel, T. Simeonov, and J. Rhodes, 'HELIOS-2 Methods Manual'. Studsvik, Dec. 16, 2011.
[14] D. Litskevich, B. Merk, and S. Atkinson, 'Verification of the current coupling collision probability method with orthogonal flux expansion for the case of single cell', *Progress in Nuclear Energy*, vol. 120, p. 103219, Feb. 2020, doi: 10.1016/j.pnucene.2019.103219.
[15] D. Litskevich and B. Merk, 'SP3 Solution versus Diffusion Solution in Pin-by-Pin Calculations and Conclusions Concerning Advanced Methods', *Journal of Computational and Theoretical Transport*, vol. 43, pp. 214–239, 2014.
[16] B. Merk and R. Koch, 'On the influence of spatial discretization in LWR cell- and lattice calculations with HELIOS 1.9', *Annals of Nuclear Energy*, vol. 35, no. 8, pp. 1492–1501, 2008, doi: https://doi.org/10.1016/j.anucene.2008.01.022.
[17] E. E. (Elmer E. Lewis and W. F. Miller, *Computational methods of neutron transport*. New York : Wiley, 1984.
[18] G. H. Golub and C. F. Van Loan, *Matrix Computations (3rd Ed.)*. Baltimore, MD, USA: Johns Hopkins University Press, 1996.
[19] M. A. Smith, E. E. Lewis, and B.-C. Na, 'Benchmark on deterministic 2-D MOX fuel assembly transport calculations without spatial homogenization', *Progress in Nuclear Energy*, vol. 45, no. 2, pp. 107–118, 2004, doi: https://doi.org/10.1016/j.pnueene.2004.09.003.
[20] N. Z. Cho, 'Benchmark Problems in Reactor and Particle Transport Physics'. http://nurapt.kaist.ac.kr/benchmark/ (accessed Oct. 27, 2020).
[21] P. K. Romano, N. E. Horelik, B. R. Herman, A. G. Nelson, B. Forget, and K. Smith, 'OpenMC: A state-of-the-art Monte Carlo code for research and development', *Annals of Nuclear Energy*, vol. 82, pp. 90–97, 2015, doi: https://doi.org/10.1016/j.anucene.2014.07.048.

[22] ‘Multi-Group Cross Section Generation — OpenMC Documentation’. https://openmc.readthedocs.io/en/stable/pythonapi/mgxs.html#openmc.mgxs.GROUP_STRUCTURES (accessed Dec. 12, 2019).
[23] U. Ayachit, *The ParaView Guide: A Parallel Visualization Application*. USA: Kitware, Inc., 2015.